


 Cite this: *RSC Adv.*, 2026, 16, 12737

Ferrite-based materials for anticorrosion: comparative study of ZnFe_2O_4 , CuFe_2O_4 , and $\text{SrFe}_{12}\text{O}_{19}$

 Tarek Alammam,^{*a} Mahmoud A. Bedair,^{ID *b} Nadezhda A. Andreeva,^{ID c} Faisal Al-Odail,^a Mohammed A. Alkhalifah,^a Medhat E. Owda,^d Vitaly V. Chaban^{ID e} and Ahmed M. Abuelela^{*a}

Three chitosan ferrite nanoparticles— ZnFe_2O_4 , CuFe_2O_4 , and $\text{SrFe}_{12}\text{O}_{19}$ —were synthesized *via* an ultrasound-assisted PEG route, yielding phase-pure products with controlled morphologies. Structural and compositional analyses confirmed phase purity, tailored morphology, and mesoporosity across systems for cubic spinel ZnFe_2O_4 and cuprospinel CuFe_2O_4 . In contrast, $\text{SrFe}_{12}\text{O}_{19}$ exhibited coexistence of hexagonal M-type ferrite and rhombohedral $\alpha\text{-Fe}_2\text{O}_3$, indicating a multiphase nature. These nanoparticles were incorporated into chitosan-ferrite nanocomposites and evaluated as corrosion inhibitors for carbon steel in 1.0 M HCl *via* potentiodynamic polarization (PDP), electrochemical frequency modulation (EFM), and electrochemical impedance spectroscopy (EIS). All of the techniques revealed concentration-dependent inhibition, with ZnFe_2O_4 -based composites consistently demonstrating the highest efficiencies (up to 98.73% by PDP, 94.35% by EFM, and 97.38% by EIS). The inhibition mechanism was identified as mixed-type, primarily affecting the cathodic reaction, supported by causality factors and impedance parameters such as increased R_{ct} and decreased C_{dl} . Adsorption modeling showed strong monolayer behavior with spontaneous composite–metal surface interaction, validated by Langmuir fitting and ΔG_{ads}° values ($\sim -28 \text{ kJ mol}^{-1}$). These results highlight the performance of ultrasound-engineered ferrite nanocomposites in forming protective films and reducing acid-induced corrosion, underscoring their application potential in advanced coating systems.

 Received 24th October 2025
 Accepted 22nd February 2026

DOI: 10.1039/d5ra08173d

rsc.li/rsc-advances

1. Introduction

Ferrites are a broad class of magnetic oxides with versatile crystal structures, most notably spinel and hexagonal, that have traditionally found use in magnetic recording, permanent magnets, and power electronics. In recent years, however, nanostructured ferrites have emerged as promising anticorrosion materials, particularly when incorporated into protective coatings for metallic substrates. Their chemical inertness, thermal stability, and ability to form passive barrier layers make them ideal candidates for corrosion inhibition in aggressive environments.¹ The nanoscale morphology of ferrites enhances surface reactivity and dispersion within polymeric matrices,

improving coating adhesion and reducing electrolyte permeability.²

Spinel ferrites such as ZnFe_2O_4 and CuFe_2O_4 , and hexagonal ferrites like $\text{SrFe}_{12}\text{O}_{19}$, exhibit tailored cation distributions that influence their electrochemical behavior and corrosion resistance. Through composition engineering and controlled synthesis, ferrite nanoparticles can be optimized to suppress anodic and cathodic reactions, promote passivation, and extend the service life of coated metals.³ These attributes position ferrites as environmentally friendly alternatives to toxic pigments like chromates, offering multifunctional protection in industrial, marine, and infrastructure applications. Zinc ferrite (ZnFe_2O_4) is a normal spinel ferrite with a cubic crystal structure, exhibiting ferromagnetic behavior and a Néel temperature of approximately 858 K. Beyond its magnetic characteristics, ZnFe_2O_4 has gained attention as a promising anticorrosion pigment due to its chemical stability, thermal resistance, and ability to inhibit corrosion when incorporated into protective coatings.⁴ The spinel structure, comprising Zn^{2+} and Fe^{3+} ions distributed over tetrahedral and octahedral sites, contributes to its durability and passivation behavior in aggressive environments. Recent studies have demonstrated that ZnFe_2O_4 nanoparticles, when embedded in epoxy or styrene-acrylate matrices,

^aDepartment of Chemistry, College of Science, King Faisal University, Al-Ahsa 31982, Saudi Arabia. E-mail: talammar@kfu.edu.sa; aabuelela@kfu.edu.sa

^bDepartment of Chemistry, College of Science, University of Bisha, P.O. Box 511, Bisha, 61922, Saudi Arabia. E-mail: mbedair@ub.edu.sa; m_bedier@yahoo.com

^cPeter the Great St. Petersburg Polytechnic University, Saint Petersburg, Russia

^dDepartment of Chemistry, Faculty of Science, Al-Azhar University, Nasr City, 11884, Cairo, Egypt

^eIndependent Scientist, Saint Petersburg, Russian Federation



enhance the corrosion resistance of coated metal substrates by forming hydroxide layers that suppress electrochemical degradation.⁵ Additionally, its nanoscale morphology and high surface area improve pigment dispersion and barrier properties, making ZnFe_2O_4 a viable candidate for multifunctional coatings.⁶

Copper ferrite (CuFe_2O_4) is an inverse spinel ferrite with a tetragonal crystal structure, known for its thermal stability, magnetic properties, and chemical inertness. These attributes make CuFe_2O_4 a compelling candidate for anticorrosion coatings, particularly in harsh environments. The unique cation distribution – Cu^{2+} ions occupying octahedral sites and Fe^{3+} ions distributed across both tetrahedral and octahedral positions – contributes to its structural robustness and passivation behavior. Recent studies have demonstrated that CuFe_2O_4 nanoparticles, when incorporated into silicone-based or epoxy resin matrices, significantly enhance the corrosion resistance of coated metal substrates by forming compact barrier layers and promoting hydrophobicity.^{7,8} The presence of Cu^{2+} ions may also contribute to localized cathodic protection, while the ferrite matrix impedes electrolyte penetration. Furthermore, CuFe_2O_4 's nanoscale morphology and magnetic recoverability offer additional advantages for smart coating systems and multifunctional surface protection.⁹

Strontium hexaferrite ($\text{SrFe}_{12}\text{O}_{19}$) is an M-type hexagonal ferrite known for its high coercivity, thermal stability, and chemical inertness. These properties make it a strong candidate for anticorrosion coatings, especially in environments requiring long-term durability. The magnetoplumbite structure of $\text{SrFe}_{12}\text{O}_{19}$, with Fe^{3+} ions occupying five distinct crystallographic sites, contributes to its robust lattice and resistance to chemical attack. When incorporated into polymeric matrices such as epoxy or polyaniline composites, $\text{SrFe}_{12}\text{O}_{19}$ nanoparticles enhance barrier performance by reducing electrolyte permeability and promoting passive layer formation on metal surfaces.¹⁰ Recent studies have shown that $\text{SrFe}_{12}\text{O}_{19}$ -based nanocomposites exhibit excellent adhesion, low charge-transfer resistance, and high cyclic stability, making them suitable for multifunctional coatings that combine magnetic and protective functions.¹⁰ Additionally, its compatibility with conductive polymers and carbon-based additives allows for tailored electrochemical behavior, further improving corrosion resistance.¹¹

Traditionally, the solid-state reaction technique has been widely employed for ferrite synthesis; however, it presents several limitations, including high temperature requirements, large crystallite sizes, and poor compositional homogeneity.¹² To overcome these drawbacks, recent studies have investigated various wet chemical methods for synthesizing ferrite materials such as ZnFe_2O_4 , CuFe_2O_4 , and $\text{SrFe}_{12}\text{O}_{19}$ – notably sol-gel, coprecipitation, and microwave-assisted hydrothermal techniques. Among these, ultrasound-assisted synthesis has emerged as a mild, energy-efficient, and versatile approach for producing high-purity, crystalline, and compositionally homogeneous ferrites. For example, Chen *et al.* synthesized $\text{ZnFe}_2\text{O}_4@ \text{TiO}_2$ core-shell structures *via* ultrasonic treatment, achieving enhanced phase control and photocatalytic activity.¹³

Meenu *et al.* reported the ultrasound-enabled fabrication of CuFe_2O_4 -Ag nanocomposites within hydrogel matrices, demonstrating improved dispersion and dye degradation performance.¹⁴ Similarly, Palomino *et al.* achieved monodisperse $\text{SrFe}_{12}\text{O}_{19}$ nanoparticles through sonochemical processing, highlighting the method's efficacy for complex hexaferrites.¹⁵ These findings underscore the adaptability of ultrasound-assisted synthesis across both simple binary oxides and structurally intricate spinel and hexaferrite systems.

Herein, we report the synthesis of ZnFe_2O_4 , CuFe_2O_4 , and $\text{SrFe}_{12}\text{O}_{19}$ nanoparticles *via* a versatile ultrasound-assisted polyethylene glycol (PEG) route. This method enabled the formation of phase-pure, crystalline ZnFe_2O_4 and CuFe_2O_4 ferrites with controlled morphology and dispersion, while $\text{SrFe}_{12}\text{O}_{19}$ was obtained as a multiphase material comprising dominant hexagonal magnetoplumbite and a minor α - Fe_2O_3 phase. The structural characteristics of the synthesized nanoparticles were systematically investigated, and their performance as corrosion inhibitors was evaluated. To comprehensively assess their anticorrosion potential, electrochemical techniques and adsorption modeling were employed, complemented by density functional theory (DFT) calculations to elucidate the molecular interactions and reactivity at the metal-inhibitor interface.

2. Experimental Section

2.1 Materials

All reagents used were commercially available and directly employed without further purification. Iron(III) nitrate nonahydrate (99%) was purchased from Riedel-deHaen, sodium hydroxide (99%), zinc acetate-2-hydrate (99%) from FARCO, copper(II) acetate monohydrate (99%), strontium nitrate (99%), ethanol (p.a.), polyethylene glycol 6000 (PEG 6000) (99%) from Sigma-Aldrich.

2.2 Synthetic procedures

2.2.1 Synthesis of ZnFe_2O_4 , CuFe_2O_4 , and $\text{SrFe}_{12}\text{O}_{19}$. Spinel ZnFe_2O_4 , CuFe_2O_4 , and hexaferrite $\text{SrFe}_{12}\text{O}_{19}$ were synthesized using a PEG-assisted sonochemical precipitation approach. Stoichiometric amounts of $\text{Fe}(\text{NO}_3)_3 \cdot 9\text{H}_2\text{O}$ (0.33, 0.4, and 0.6 g), $\text{Zn}(\text{CH}_3\text{COO})_2 \cdot 2\text{H}_2\text{O}$ (0.12 g), $\text{Cu}(\text{CH}_3\text{COO})_2 \cdot \text{H}_2\text{O}$ (0.1 g), and $\text{Sr}(\text{NO}_3)_2$ (0.2 g) were individually dissolved in 5 mL of deionized water containing PEG 600 (0.5 g), followed by stirring for 10 min in sealed glass vessels at room temperature. Sodium hydroxide (0.25 g) was then introduced to each solution, and the mixtures were stirred vigorously for an additional 30 min. Each reaction mixture underwent sonication for 3 h in an ultrasonic bath (LUC-405, DAIHAN LABTECH Co. Ltd; 60 kHz, 350 W). The resulting precipitates were separated by centrifugation, thoroughly washed with distilled water, and dried at 100 °C for 3 h. Finally, calcination in air at 500 °C for 3 h yielded phase-pure ZnFe_2O_4 and CuFe_2O_4 . $\text{SrFe}_{12}\text{O}_{19}$ required higher thermal treatment and was calcined at 700 °C for 3 h to achieve the desired hexaferrite phase.



2.2.2 Synthesis of chitosan/metal oxide nanocomposites.

For the preparation of chitosan/metal oxide nanocomposites, 1 g of chitosan was dissolved in 50 mL of deionized water containing 2.5 mL of 5% acetic acid. The solution was stirred continuously for 4 h until a homogeneous viscous gel was formed. Subsequently, 0.3 g of ZnFe₂O₄, CuFe₂O₄, or SrFe₁₂O₁₉ powder was separately added to the chitosan solution and stirred for 24 h to ensure uniform dispersion. The mixture was then neutralized using 100 mL of 2% NaOH, followed by centrifugation and repeated washing with distilled water. The resulting Ch–Oxide nanocomposites were dried in an oven at 100 °C for 3 h.

2.3 Characterization

The phase composition and structural properties of the metal oxide nanoparticles were determined using X-ray diffraction (XRD), performed on a Seifert 3003TT diffractometer with copper K α radiation as the source.

Transmission Electron Microscopy (TEM), conducted with a JEOL GEM-1010 system, provided high-resolution imaging of nanoparticle morphology. Elemental analysis was carried out concurrently using Energy-Dispersive X-ray spectroscopy (EDX).

The specific surface area and adsorption–desorption characteristics of the sample were assessed at cryogenic temperatures using a Quantachrome instrument (USA), featuring TouchWin software for data acquisition and analysis.

2.4 Electrochemical measurements

Electrochemical tests were conducted using a Gamry REF600-16084 potentiostat with data processed using Echem Analyst 2 (Framework v7.10.4). A standard three-electrode setup (100 mL capacity) was used, consisting of a polished steel working electrode (1.0 cm²), platinum wire counter electrode, and saturated Ag/AgCl reference electrode. Tests were conducted in 1 M HCl at 30 \pm 1 °C, with varying concentrations (40 to 400 ppm) of chitosan/metal oxide nanocomposites. Prior to testing, the working electrode was immersed in the test solution and left to stabilize for 3600 seconds to reach a stable open circuit potential (OCP). Electrochemical Frequency Modulation (EFM) was performed with a foundational frequency of 0.1 Hz, along with multipliers of 2.0 and 5.0, and an amplitude set at 10 mV.¹⁶ The utilization of these parameters facilitated the examination of inhibitor adsorption kinetics and non-faradaic phenomena.¹⁷ Concurrently, Electrochemical Impedance Spectroscopy (EIS) was executed at the open circuit potential (OCP) employing a 10 mV alternating current (AC) signal across a frequency spectrum ranging from 100 kHz to 0.01 Hz. Potentiodynamic polarization (PDP) was carried out by scanning the potential \pm 250 mV with respect to OCP at a scan rate of 0.5 mV s⁻¹. Inhibition efficiency was calculated from the following equations:¹⁸

$$\eta_{\text{P,EFM}}\% = 100 \left(1 - \frac{i_{\text{inh}}^{\text{corr}}}{i_{\text{blank}}^{\text{corr}}} \right) \quad (1)$$

2.5 Theoretical methodology and methods

Plane-wave Kohn–Sham density functional theory (KS-DFT) calculations with pure PBEPBE exchange–correlation functional,¹⁹ implemented into Quantum Espresso program package, version 7.1,²⁰ were used to optimize the geometries of the NPs. The van der Waals correction (DFT-D) was applied to realistically represent van der Waals forces in KS-DFT calculations.²¹ The plane-wave energy cut-off was set to 75 Ry for the zinc-containing system and 45 Ry for all other systems. Due to the accuracy limitations of pure functionals, the global reactivity parameters and partial atomic charges were deliberately obtained *via* hybrid density functional theory (HDFT). The M11 exchange–correlation *meta*-GGA functional was hereby used.²² To solve d-element-containing compositions, we employed the Stuttgart/Dresden effective core potentials. The dispersive attraction was included inherently.^{23,24} The convergence criterion within the self-consistent field procedure was set to 10⁻⁷ hartree. The implicit solvent water was used because the simulated NPs are expected to neutralize corrosion promoters in their aqueous environment. The partial atomic electrostatic charges were derived by fitting the HDFT-derived electrostatic potential in the system using the Merz–Kollman algorithm. The HDFT calculations were conducted in Gaussian'09D.²⁵ The reported calculations were carried out using an implicit water model, which represents the solvent as a matterless polarizable continuum at effectively low ionic strength. In particular, the 1 M HCl environment of the corrosion experiments is not hereby explicitly modeled. No hydronium cations and no chloride anions are present. Thereby no electric double layer is formed at the metal/solution interface. The modeled inhibitor is treated in its neutral form. In tun, under the strongly acidic experimental conditions it is expected to exist predominantly in protonated and fractionally ion-paired states. As a consequence, the computed electronic descriptors and adsorption-related properties should be regarded as qualitative indicators of the intrinsic reactivity of the inhibitor molecules. A fully quantitative description of the 1 M HCl medium requires explicit treatment of H⁺/H₃O⁺ and Cl⁻, high ionic strength, and interfacial charging, which is beyond the current scope.

3. Results and discussion

3.1 Morphology, crystallinity, and porosity of ferrite nanoparticles

Powder X-ray diffraction (XRD) analysis was employed to assess the phase composition and purity of the synthesized samples, as illustrated in Fig. 1. The diffraction pattern of ZnFe₂O₄ matched perfectly with the reference data (JCPDS Card No. 01-082-1042), confirming the formation of cubic spinel zinc ferrite without any detectable secondary phases or impurity peaks. Similarly, the XRD pattern of CuFe₂O₄ revealed that the dominant phase was cuprospinel, with all diffraction angles corresponding to the standard card [JCPDS No. 034-0425], and no evidence of extraneous crystal phases. Notably, no peak splitting, broadening, or asymmetry-typically associated with tetragonal distortion-was observed in the diffraction pattern.



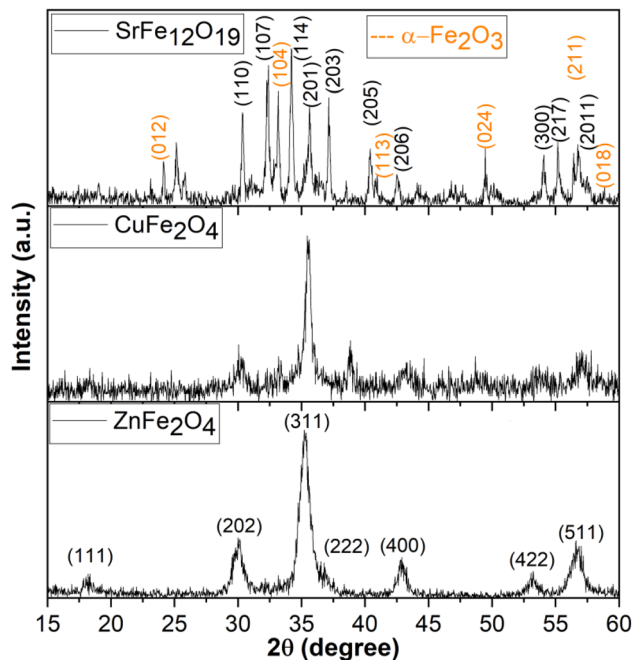


Fig. 1 XRD patterns recorded for the ZnFe_2O_4 , CuFe_2O_4 , and $\text{SrFe}_{12}\text{O}_{19}$ samples.

Detailed peak analysis of $\text{SrFe}_{12}\text{O}_{19}$ indicated that the majority of reflections aligned with the hexagonal space group $P6_3/mmc$, while a subset of peaks matched the rhombohedral space group $R\bar{3}c$. This coexistence of reflections suggests the presence of two distinct crystalline phases within the synthesized material. Specifically, the lattice planes (110), (112), (107), (114), (201), (203), (205), (206), (300), (217), (2011), (220), and (2013) are characteristic of M-type hexaferrites with a hexagonal structure (JCPDS Card No. 79-1411). The second phase, attributed to $\alpha\text{-Fe}_2\text{O}_3$ with rhombohedral symmetry, is evidenced by peaks at (012), (113), (024), (211), (018), and (224), corresponding to the $R\bar{3}c$ space group (JCPDS Card No. 33-0664). By comparing the integrated intensities of the $\alpha\text{-Fe}_2\text{O}_3$ reflections to those of the dominant $\text{SrFe}_{12}\text{O}_{19}$ peaks, the $\alpha\text{-Fe}_2\text{O}_3$ phase was estimated to constitute approximately 11 wt% of the total crystalline content. The average crystallite size of the synthesized composite materials was calculated using Scherrer's equation (eqn (2)):

$$D = \frac{k\lambda}{\beta \cos \theta} \quad (2)$$

where D = crystallite size, k = shape factor, λ = wavelength of X-ray, β = (FWHM) full width at half maximum of the peak in radians, θ = Bragg diffraction angle. The estimated crystallite sizes were approximately 11.70 nm for ZnFe_2O_4 , 15.80 nm for CuFe_2O_4 , and 38.00 nm for $\text{SrFe}_{12}\text{O}_{19}$.

The elemental composition of the synthesized ZnFe_2O_4 , CuFe_2O_4 , and $\text{SrFe}_{12}\text{O}_{19}$ samples was evaluated using energy dispersive X-ray spectroscopy (EDX). As shown in Fig. 2, the spectra confirm the presence of the respective constituent elements: Zn, Cu, Sr, Fe, and O, consistent with the expected stoichiometry of each ferrite system. Importantly, no extraneous impurity bands were detected in any of the spectra, affirming

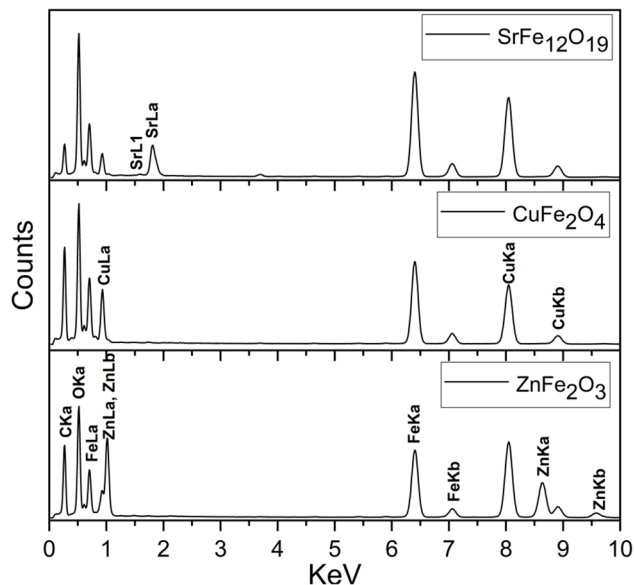


Fig. 2 EDX spectra recorded for the ZnFe_2O_4 , CuFe_2O_4 , and $\text{SrFe}_{12}\text{O}_{19}$ samples.

the phase purity of the synthesized samples. Minor C peaks were observed, attributed to the carbon support film used in the TEM sample preparation, and are not indicative of contamination from synthesis.

The TEM was conducted to investigate the morphology, crystallite dimensions, and agglomeration behavior of the synthesized ferrite samples (Fig. 3). ZnFe_2O_4 nanoparticles (Fig. 3a) exhibit predominantly spherical to quasi-spherical morphologies, with diameters ranging from ~ 5 to 20 nm and a notable concentration within the 10–15 nm range. Individual crystallites frequently assemble into chain-like and flower-shaped polycrystalline aggregates with average sizes of ~ 100 –120 nm, formed through oriented attachment and surface energy minimization. CuFe_2O_4 nanoparticles (Fig. 3b) display nearly spherical to faceted morphologies, reflecting shape anisotropy likely influenced by local growth conditions. Primary particle sizes measure ~ 10 –30 nm, while TEM images reveal densely packed clusters with average dimensions of ~ 120 –140 nm, suggesting stronger agglomeration compared to ZnFe_2O_4 . This clustering is likely driven by magnetic dipole interactions, which promote particle–particle attraction and reduce dispersion. $\text{SrFe}_{12}\text{O}_{19}$ particles (Fig. 3c) exhibit plate-like and slightly elongated morphologies, with occasional faceted edges. These features align with the intrinsic hexagonal magnetoplumbite structure, where anisotropic growth along specific crystallographic axes dominates. Particle sizes span ~ 30 –80 nm, and the relatively well-defined edges suggest high crystallinity. However, the presence of a secondary $\alpha\text{-Fe}_2\text{O}_3$ phase, confirmed by XRD, indicates that the observed morphology may also include interspersed hematite crystallites. Hematite typically forms smaller, pseudo-plate or granular particles that can adhere to or embed within the larger hexaferrite plates, subtly altering surface texture and particle boundaries. As a result, the morphology of $\text{SrFe}_{12}\text{O}_{19}$ should be



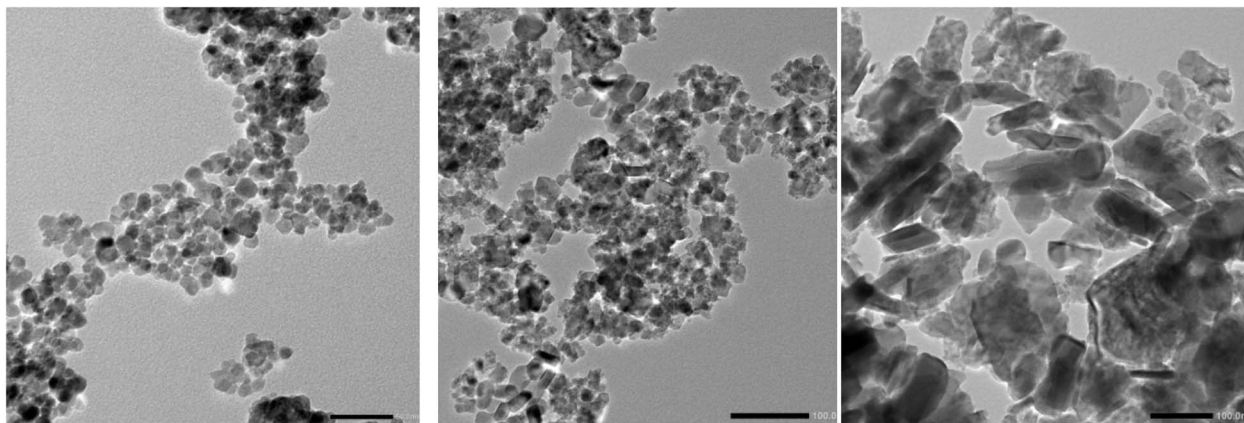


Fig. 3 TEM images of ZnFe_2O_4 (left), CuFe_2O_4 (middle) and $\text{SrFe}_{12}\text{O}_{19}$ (right) NPs.

understood as a composite of dominant hexaferrite plates with embedded or attached hematite crystallites, a structural complexity that may influence surface accessibility, particle-particle interactions, and ultimately electrochemical behavior.²⁶ Overall, TEM analysis confirms distinct morphological characteristics across the ferrite systems: moderate agglomeration in ZnFe_2O_4 , stronger clustering in CuFe_2O_4 , and relatively uniform

dispersion in $\text{SrFe}_{12}\text{O}_{19}$. The hierarchical structures observed are expected to play a critical role in determining surface accessibility, pigment packing, and electrolyte diffusion, thereby influencing inhibition efficiency and overall coating performance. Furthermore, the particle sizes observed through TEM analysis were found to be in good agreement with the

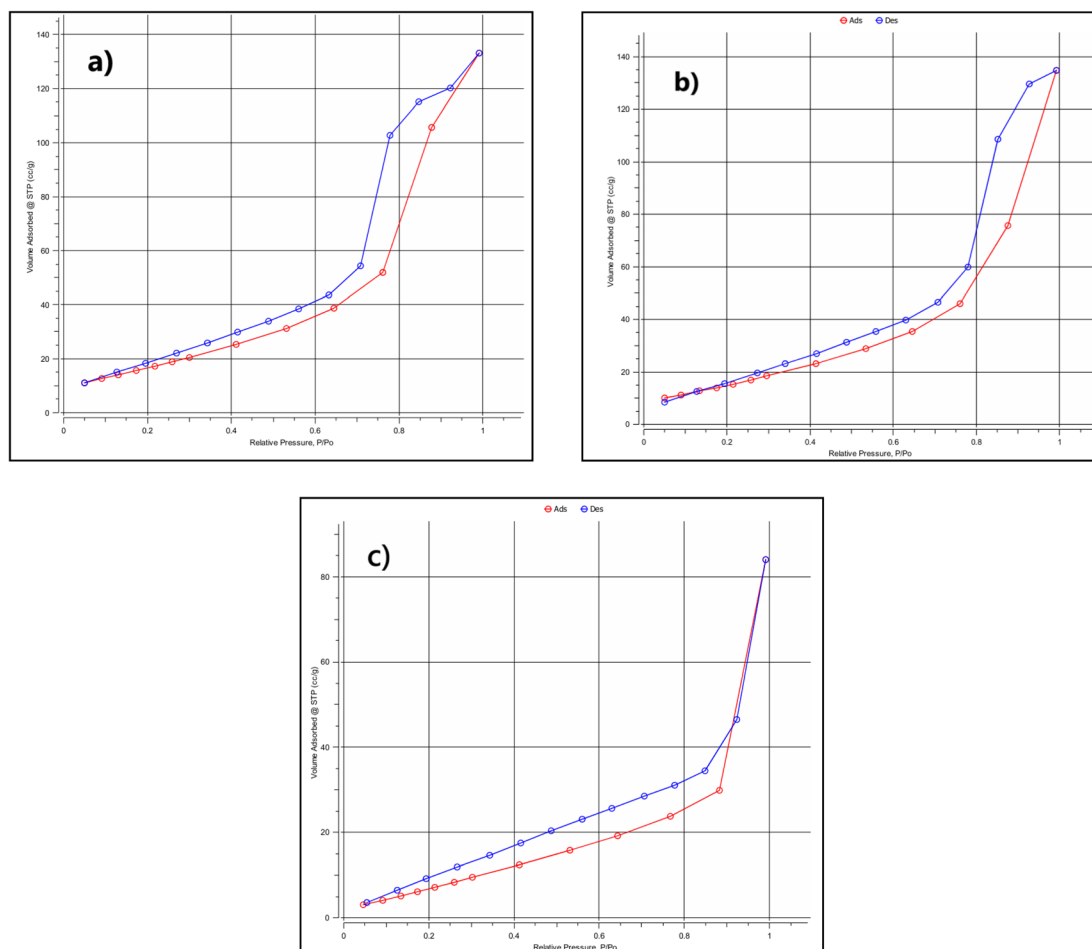


Fig. 4 N_2 adsorption–desorption of the of (a) ZnFe_2O_4 , (b) CuFe_2O_4 and (c) $\text{SrFe}_{12}\text{O}_{19}$ samples.



crystallite sizes estimated from XRD data, supporting the reliability of the measurements.

The N_2 adsorption-desorption isotherms of $ZnFe_2O_4$, $CuFe_2O_4$, and $SrFe_{12}O_{19}$ uniformly exhibit type IV profiles with H3 hysteresis loops, consistent with mesoporous structures containing slit-like pores formed *via* particle agglomeration (Fig. 4). These hysteresis loops, arising from the divergence between adsorption and desorption branches, affirm the presence of interconnected pore networks that facilitate capillary condensation and surface accessibility—key factors in optimizing coating performance. In all systems, initial uptake at low relative pressures ($P/P_0 < 0.3$) corresponds to monolayer adsorption, followed by a steep increase near $P/P_0 \approx 0.8$ – 0.9 associated with capillary condensation in mesopores.

For $ZnFe_2O_4$, the BET surface area was measured at $65.8 \text{ m}^2 \text{ g}^{-1}$, which, although lower than some reported maxima – such as the $78.9 \text{ m}^2 \text{ g}^{-1}$ for $ZnFe_2O_4$ obtained *via* ultrasound-assisted synthesis using glucose precursors²⁷ – remains comparatively high and exceeds many values reported for conventional synthesis routes. For instance, Jadhav *et al.* reported a BET value of only $2.27 \text{ m}^2 \text{ g}^{-1}$ for $ZnFe_2O_4$ prepared by a sol-gel auto-combustion method using urea as a chelating agent.²⁸ Similarly, Tomina *et al.* obtained a BET surface area of approximately $26 \text{ m}^2 \text{ g}^{-1}$ for $ZnFe_2O_4$ synthesized *via* a precipitation method assisted by citric acid as a capping agent.²⁹ The slightly reduced surface area observed in our study is attributed to particle agglomeration evident in TEM images, which limits external surface exposure and pore accessibility. Nevertheless, the material exhibits a well-developed mesoporous structure, and the achieved surface area is sufficient to support its intended anticorrosion application.

$CuFe_2O_4$ displayed a BET surface area of $54.1 \text{ m}^2 \text{ g}^{-1}$, which lies within the broad literature range (9 – $160 \text{ m}^2 \text{ g}^{-1}$) and is higher than several values reported for conventional methods such as thermal decomposition ($18.2 \text{ m}^2 \text{ g}^{-1}$) or precipitation ($24.1 \text{ m}^2 \text{ g}^{-1}$).³⁰ The relatively small BJH-derived average pore diameter of 1.93 nm , though lower than the typical 4 – 8 nm range, is consistent with slit-like mesopores indicated by the H3 hysteresis loop. This discrepancy is explained by synthesis-specific factors—rapid nucleation, restricted grain growth, and magnetic dipole-driven clustering—that reduce interparticle spacing and limit pore expansion. Larger mesopores reported in literature generally arise from template-assisted or high-temperature calcination routes, which differ significantly from the present synthesis conditions.^{31–33}

$SrFe_{12}O_{19}$ exhibited a BET surface area of $41.7 \text{ m}^2 \text{ g}^{-1}$ and a BJH pore size of 1.92 nm . While the nearly identical pore size values for $CuFe_2O_4$ and $SrFe_{12}O_{19}$ appear statistically unusual, they are more likely artifacts of the BJH method, which assumes cylindrical pore geometry and is less accurate for slit-like or irregular pores.³⁴ In $SrFe_{12}O_{19}$, the low pore volume ($0.12 \text{ cm}^3 \text{ g}^{-1}$) and plate-like morphology suggest minimal mesoporosity, with the measured pore size reflecting surface voids or edge effects rather than intrinsic pore structure.³⁵

Correlation between TEM and BET analyses confirms that particle agglomeration plays a decisive role in reducing surface area compared to literature maxima. TEM revealed moderate

Table 1 Textural properties derived from BET and BJH analyses

Pore radius (nm)	Pore volume ($\text{cm}^3 \text{ g}^{-1}$)		
	$ZnFe_2O_4$	$CuFe_2O_4$	$SrFe_{12}O_{19}$
1.92	0.0085	0.0105	0.0076
2.58–2.59	0.0207	0.0232	0.0150
3.72–3.76	0.0454	0.0444	0.0246
6.51–6.72	0.1596	0.1067	0.0365
56–71	0.2036	0.2014	0.1242

clustering in $ZnFe_2O_4$, stronger aggregation in $CuFe_2O_4$, and relatively uniform dispersion in $SrFe_{12}O_{19}$. These morphological traits directly influenced BET values, as agglomeration reduces accessible surface area and narrows pore distributions, consistent with prior reports.

To provide quantitative insight, representative BJH adsorption pore volume data points are presented in Table 1. These values highlight the evolution of pore volume across different regimes: $ZnFe_2O_4$ and $CuFe_2O_4$ exhibit higher pore volumes and narrower distributions, consistent with their dispersed nanoparticle morphologies, whereas $SrFe_{12}O_{19}$ shows broader pores and lower overall volume, in agreement with its aggregated plate-like structure. Although $ZnFe_2O_4$, $CuFe_2O_4$, and $SrFe_{12}O_{19}$ were synthesized under identical ultrasound-assisted PEG conditions, the observed differences in BET surface area and pore size distribution arise from the intrinsic crystallographic structures, cation chemistry, and agglomeration tendencies of each ferrite system. $ZnFe_2O_4$, with its cubic spinel framework, favors quasi-spherical crystallites that assemble into moderate aggregates, yielding relatively high surface area. In contrast,

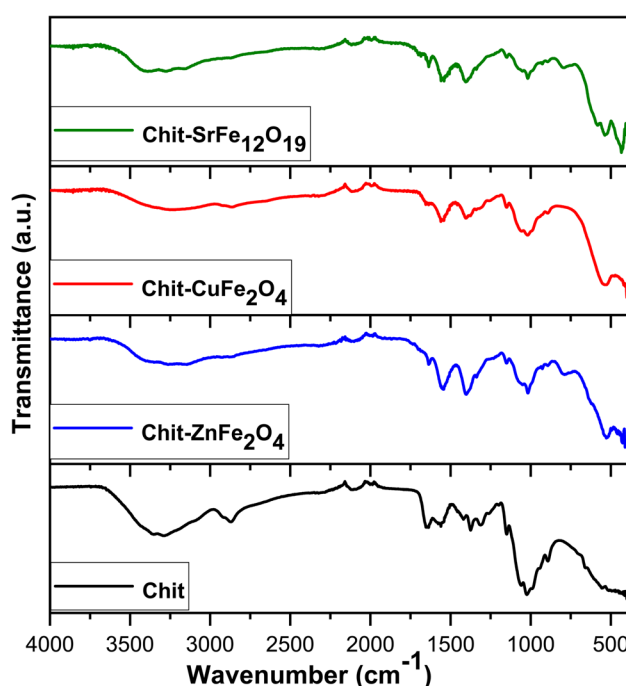


Fig. 5 FTIR spectra of Chit, Chit- $ZnFe_2O_4$ NPs, Chit- $CuFe_2O_4$ NPs, Chit- $SrFe_{12}O_{19}$ NPs.



CuFe_2O_4 exhibits stronger magnetic dipole interactions that promote clustering, thereby reducing accessible surface area and narrowing pore dimensions. $\text{SrFe}_{12}\text{O}_{19}$, dominated by anisotropic plate-like growth and the coexistence of $\alpha\text{-Fe}_2\text{O}_3$, shows minimal mesoporosity and lower pore volume due to structural packing constraints. Thus, the textural properties are not solely determined by external synthesis parameters but by the interplay between synthesis conditions and material-specific growth mechanisms. These differences in morphology and porosity directly influence pigment dispersion, interfacial bonding, and electrolyte diffusion, thereby shaping the anti-corrosion performance of the resulting nanocomposites.^{24,25}

FTIR analysis was performed to investigate the chemical interactions between chitosan and ferrite nanoparticles in the synthesized composites: **Chit- ZnFe_2O_4** , **Chit- CuFe_2O_4** , and **Chit-**

$\text{SrFe}_{12}\text{O}_{19}$ (Fig. 5). The spectra were recorded in the range of $4000\text{--}400\text{ cm}^{-1}$ and compared with pure chitosan (Chit) to identify characteristic functional groups and confirm successful incorporation of ferrite phases. All samples exhibited a broad absorption band around 3400 cm^{-1} , corresponding to the stretching vibrations of hydroxyl (O-H) and amine (N-H) groups, which are intrinsic to the chitosan backbone. The bands near 2900 cm^{-1} were attributed to C-H stretching vibrations of aliphatic groups. A prominent peak around 1650 cm^{-1} was observed in all samples, associated with the amide I (C=O) stretching vibration. Notably, this band showed slight shifts in the ferrite-modified samples, indicating possible interactions between chitosan's carbonyl groups and the metal ions of the ferrite nanoparticles. In the fingerprint region, distinct bands appeared between 500 and 600 cm^{-1} in the **Chit-**

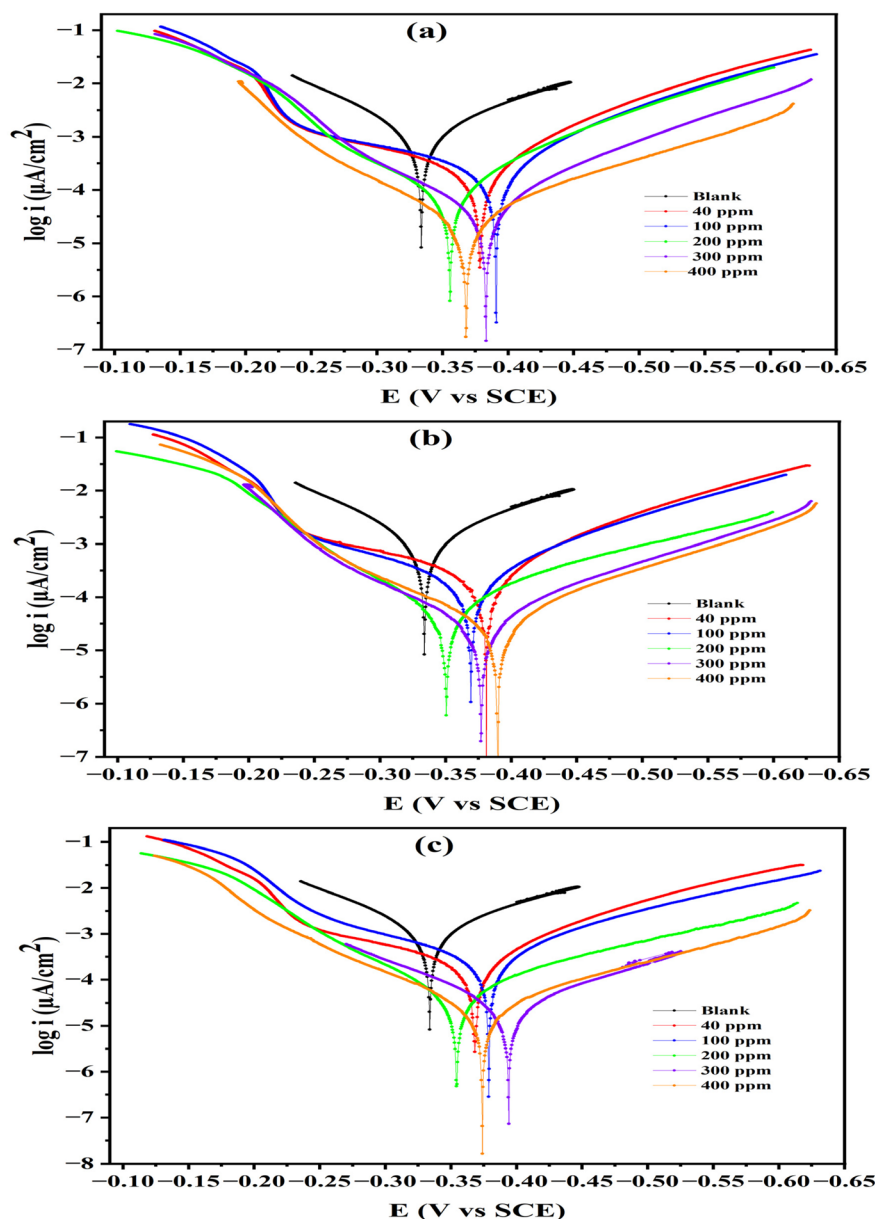


Fig. 6 Potentiodynamic polarization curves for the corrosion of carbon steel in 1.0 M HCl in absence and presence of different concentrations of (Chit- $\text{SrFe}_{12}\text{O}_{19}$ (a), Chit- CuFe_2O_4 (b) and Chit- ZnFe_2O_4 (c) composites at 30 °C.



ZnFe₂O₄, **Chit-CuFe₂O₄**, and **Chit-SrFe₁₂O₁₉** spectra, which were absent in pure chitosan. These bands are characteristic of metal–oxygen (Fe–O) stretching vibrations and confirm the presence of ferrite phases within the chitosan matrix. The variation in peak positions and intensities among the different composites reflects the influence of the specific metal ions (Sr²⁺, Cu²⁺, Zn²⁺) on the structural configuration and bonding environment. Overall, the FTIR results demonstrate successful integration of ferrite nanoparticles into the chitosan matrix and suggest chemical interactions between the polymer and the ferrite surfaces, which may influence the electrochemical behavior observed in subsequent EIS measurements.

3.2 Electrochemical measurements

3.2.1 Potentiodynamic polarization (PDP). The electrochemical behavior of carbon steel (CS) in 1.0 M HCl solution in the absence and presence of different concentrations (40, 100, 200, 300, and 400 ppm) of the synthesized **Chit-ZnFe₂O₄**, **Chit-CuFe₂O₄**, and **Chit-SrFe₁₂O₁₉** nanocomposites was investigated systematically by potentiodynamic polarization (PDP) measurements. The resulting polarization curves (Fig. 6a–c) and the extracted electrochemical parameters (Table 2) clarify the corrosion kinetics and inhibition efficiency of the composites being studied. Examination of the PDP curves indicates that addition of the chitosan–ferrite composites considerably changes the corrosion behavior of CS relative to the uninhibited acid solution. The corrosion current density (i_{corr}) drops considerably with increasing inhibitor concentration for all three composites (Table 2). This implies a considerable reduction of the overall corrosion rate, validating the effectiveness of these materials as corrosion inhibitors.^{36–38} At the same time, the inhibition efficiency ($\eta_p\%$) derived from the i_{corr} values (by using the formula given in the Experimental section) improves with concentration to arrive at impressive figures of 98.13%,

98.55%, and 98.73% for **Chit-SrFe₁₂O₁₉**, **Chit-CuFe₂O₄**, and **Chit-ZnFe₂O₄**, respectively, at the highest concentration of 400 ppm. The corrosion potential (E_{corr}) shows variation in response to the addition and concentration of inhibitors. That is, for **Chit-ZnFe₂O₄** and **Chit-CuFe₂O₄**, E_{corr} exhibits a slight shift towards more negative (cathodic) potentials as the concentration is increased, showing a notable influence on the cathodic reaction (e.g., hydrogen evolution).^{39,40} However, the shift for **Chit-SrFe₁₂O₁₉** is relatively less. The Tafel slopes (β_a and β_c) generally exhibit close value to that of the blank sample, with minor deviations based on the concentration and nature of the inhibitor. The results suggest that the inhibition mechanism probably has a mixed-type nature, having a primary influence on the cathodic process without significantly altering the inherent reaction mechanisms.^{41,42} The higher efficiency of **Chit-ZnFe₂O₄**, followed by **Chit-CuFe₂O₄** and **Chit-SrFe₁₂O₁₉**, is in accordance with the expected trends based on the textural properties and intrinsic characteristics of the ferrite nanoparticles.⁴³ The significant surface area and mesoporosity of ZnFe₂O₄ nanoparticles are expected to favor greater adsorption and better spreading of the inhibitor over the metal interface, thus forming a more efficient protective film.⁴⁴ Though CuFe₂O₄ has a lower surface area, its spinel structure and redox properties are likely to be responsible for its high inhibition efficiency. In spite of having the lowest surface area and pore volume, SrFe₁₂O₁₉ still manifests excellent inhibition, which can be related to its unique plate-like morphology and the chemical stability imparted by its hexagonal structure, possibly providing effective barrier coverage.⁴⁵

The PDP data validate that the chitosan–ferrite nanocomposites synthesized are good corrosion inhibitors for carbon steel in 1.0 M HCl. The inhibition efficiency is concentration-dependent, and the activity order (**Chit-ZnFe₂O₄** \geq **Chit-CuFe₂O₄** > **Chit-SrFe₁₂O₁₉** at higher concentrations) aligns with the physicochemical characteristics of the ferrite

Table 2 Electrochemical parameters for carbon steel dissolution in 1.0 M HCl solution containing different concentrations of the (Chit-SrFe₁₂O₁₉, Chit-CuFe₂O₄ and Chit-ZnFe₂O₄) composites obtained from polarization measurements at 30 °C^a

Inhibitor name	Conc. (ppm)	E_{corr} vs. SCE (mV)	i_{corr} ($\mu\text{A cm}^{-2}$) \pm SD	β_a (mV dec ⁻¹)	$-\beta_c$ (mV dec ⁻¹)	k (mpy)	θ	$\eta_p\%$
Blank	—	−333.7	1579.00 \pm 11.04	104.1	136.4	721.5	—	—
Chit-SrFe₁₂O₁₉	40	−378.6	349.30 \pm 7.99	202.9	113.3	159.6	0.7788	77.88
	100	−390.9	245.30 \pm 7.12	173.7	105.9	112.1	0.8446	84.46
	200	−355.7	94.46 \pm 5.35	79.49	99.65	43.16	0.9402	94.02
	300	−383.1	38.03 \pm 4.52	73.72	96.14	17.38	0.9759	97.59
	400	−367.9	29.59 \pm 2.29	83.32	121.3	13.52	0.9813	98.13
Chit-CuFe₂O₄	40	−381.0	339.70 \pm 6.52	183	183	155.2	0.7849	78.49
	100	−369.2	225.00 \pm 7.77	131.3	117.3	102.8	0.8575	85.75
	200	−350.6	75.80 \pm 4.85	82.29	141.9	34.63	0.9520	95.20
	300	−377.0	35.36 \pm 4.87	90.66	115	16.16	0.9776	97.76
	400	−389.7	22.82 \pm 3.11	76.86	103.4	10.43	0.9855	98.55
Chit-ZnFe₂O₄	40	−368.2	313.40 \pm 6.45	168.7	115.1	143.2	0.8015	80.15
	100	−378.6	216.40 \pm 6.29	103.2	116.1	98.87	0.8630	86.30
	200	−354.2	53.92 \pm 4.34	75.38	134.3	24.64	0.9659	96.59
	300	−394.0	34.68 \pm 2.15	102.5	129.3	15.85	0.9780	97.80
	400	−373.9	20.05 \pm 2.03	78.01	119	9.161	0.9873	98.73

^a E_{corr} is the corrosion potential; i_{corr} is the corrosion current density; β_a and β_c are Tafel constants for both anode and cathode; k , is the corrosion rate; θ , is the surface coverage; η_p , is the inhibition efficiency.



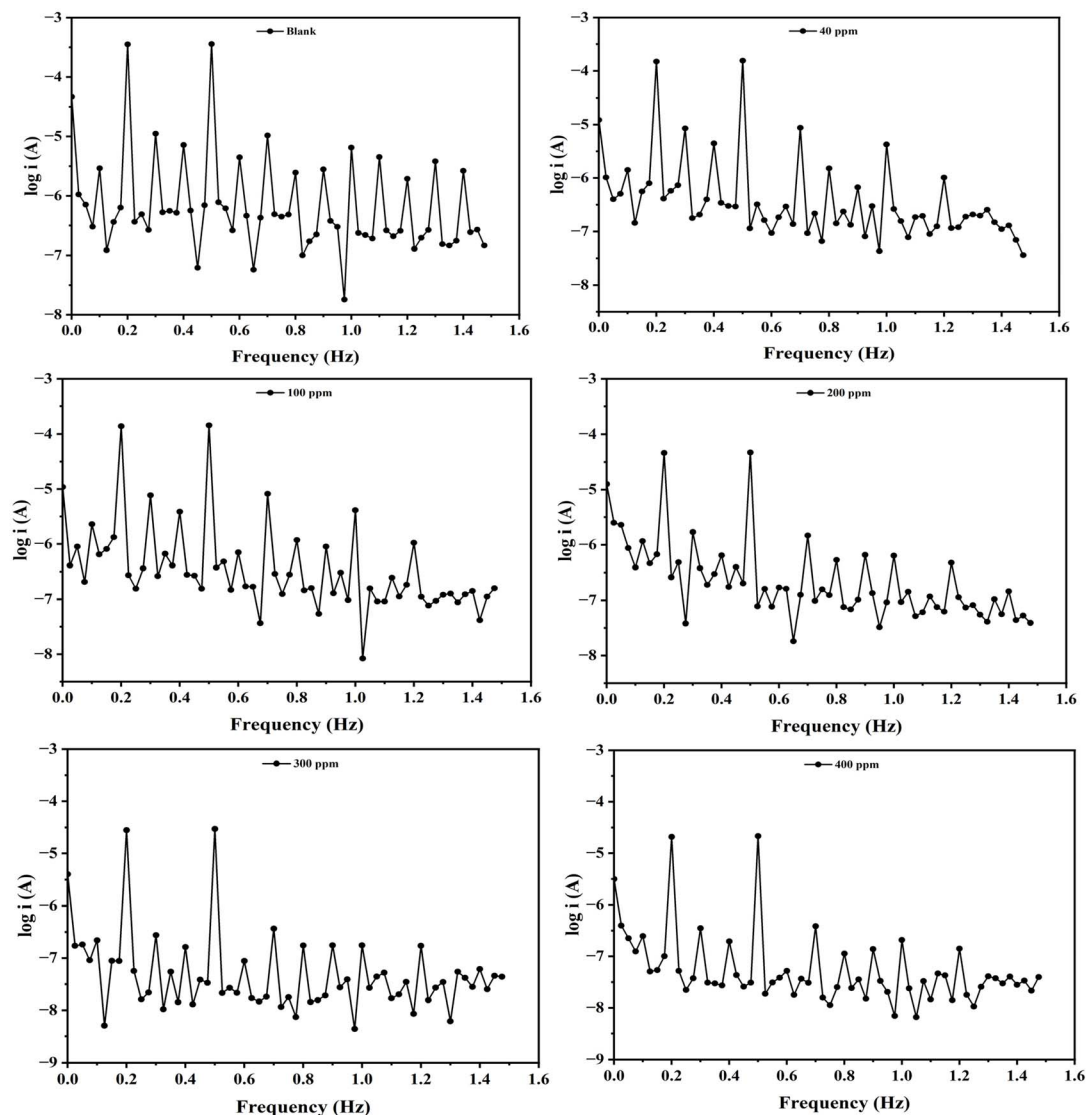


Fig. 7 Intermodulation spectra for carbon steel in 1.0 M HCl in absence and presence of different concentrations from Chit-ZnFe₂O₄ composite at 30 °C.

nanoparticles incorporated. The inhibition process seems to be through the adsorption of a protective layer onto the steel surface, inhibiting anodic dissolution and, more pronouncedly, the cathodic evolution of hydrogen.

3.2.2 Electrochemical frequency modulation (EFM). In order to get more information about the inhibition mechanism of corrosion and confirm the PDP results, Electrochemical Frequency Modulation (EFM) measurements were made. EFM is a non-destructive DC method that superimposes two small-amplitude sine waves, producing intermodulation products with amplitudes and phases dependent on the corrosion current density (i_{corr}) and Tafel parameters, without the need for previous knowledge of β_a and β_c to interpret data.^{46,47} The intermodulation spectra recorded for carbon steel in 1.0 M HCl solution, in the absence and presence of different concentrations (40, 100, 200, 300, 400 ppm) of Chit-ZnFe₂O₄, Chit-CuFe₂O₄, and Chit-SrFe₁₂O₁₉, are shown in Fig. 7, S1, S2 and

tabulated in Table 3. The spectra generally exhibit current density responses at different frequencies, including the base frequencies (f_1, f_2) and their combinations (e.g., $2f_1, 2f_2, f_1 + f_2, f_1 - f_2$).^{48,49} The amplitude of these responses is directly related to the corrosion activity. EFM-derived causality factors (CF-2 and CF-3) compare measured intermodulation currents to theoretical, with ideal values of CF-2 \approx 2.0 and CF-3 \approx 3.0.⁵⁰ The blank solution values (CF-2 = 1.574, CF-3 = 3.465) were near ideal, confirming the validity of the EFM measurements.⁵¹ With chitosan-ferrite composites addition, CF-2 and CF-3 varied around their theoretical values. These changes signify the composites affect interfacial electrochemical processes beyond simple physical blocking, suggesting kinetic modifications or complex layer formation. Examination of the EFM data shows that there are drastic changes in the corrosion behavior with the addition of inhibitors. The calculated i_{corr} values (Table 3) show a steady reduction with increasing concentration of the inhibitors for



Table 3 Electrochemical kinetic parameters obtained by EFM technique for carbon steel in the absence and presence of various concentrations of (Chit-SrFe₁₂O₁₉, Chit-CuFe₂O₄ and Chit-ZnFe₂O₄) composites in 1.0 M HCl at 30 °C^a

Inhibitor name	Conc. (ppm)	i_{corr} ($\mu\text{A cm}^{-2}$) \pm SD	β_{a} (mV dec ⁻¹)	β_{c} (mV dec ⁻¹)	CF-2	CF-3	k (mpy)	θ	$\eta_{\text{EFM}}\%$
Blank	—	739.3 \pm 5.18	124.2	162.0	1.574	3.465	337.80	—	—
Chit-SrFe₁₂O₁₉	40	437.3 \pm 5.37	137.6	216.5	1.861	2.601	199.80	0.4085	40.85
	100	307.7 \pm 6.29	84.9	100.0	2.008	3.114	140.60	0.5838	58.38
	200	193.5 \pm 5.42	100.6	115.6	1.883	3.368	88.40	0.7383	73.83
	300	67.0 \pm 3.04	111.1	120.6	1.873	2.950	30.62	0.9094	90.94
	400	59.2 \pm 3.65	117.4	140.2	2.224	3.198	27.04	0.9199	91.99
Chit-CuFe₂O₄	40	334.8 \pm 6.44	115.9	247.2	2.022	2.492	153.00	0.5471	54.71
	100	302.3 \pm 5.99	132.1	158.8	1.869	2.129	138.10	0.5911	59.11
	200	88.9 \pm 4.07	110.0	138.6	1.840	2.059	40.60	0.8798	87.98
	300	64.4 \pm 3.99	114.3	148.7	1.830	3.721	29.42	0.9129	91.29
	400	53.8 \pm 2.22	138.6	147.8	1.489	3.640	24.60	0.9272	92.72
Chit-ZnFe₂O₄	40	327.2 \pm 5.35	115.9	194.6	1.975	3.616	149.50	0.5574	55.74
	100	261.4 \pm 5.57	103.8	162.2	1.973	2.422	119.40	0.6464	64.64
	200	75.9 \pm 3.76	100.4	127.6	2.483	3.520	34.67	0.8974	89.74
	300	61.5 \pm 2.11	137.5	151.9	1.906	2.811	28.10	0.9168	91.68
	400	41.8 \pm 2.64	124.9	144.3	1.824	2.366	19.10	0.9435	94.35

^a E_{CORR} is the corrosion potential; i_{CORR} is the corrosion current density; β_{a} and β_{c} are Tafel constants for both anode and cathode; k , is the corrosion rate; θ , is the surface coverage; η_{EFM} , is the inhibition efficiency.

the three nanocomposites, similar to those found in PDP measurements. This is a clear indication of the ability of the chitosan–ferrite composites to minimize the corrosion rate of carbon steel in the acidic medium.⁵² At the same time, the inhibition efficiency ($\eta_{\text{EFM}}\%$), calculated from the i_{CORR} values, rises with concentration. Interestingly, at the highest concentration examined (400 ppm), inhibition efficiencies of 91.99%, 92.72%, and 94.35% were achieved for **Chit-SrFe₁₂O₁₉**, **Chit-CuFe₂O₄**, and **Chit-ZnFe₂O₄**, respectively. EFM-derived Tafel constants (β_{a} and β_{c}) (Table 3) are also informative. For chitosan–ferrite composites, β_{c} and β_{a} values exhibit slight changes relative to the blank. The variations of β_{a} and β_{c} indicate that the inhibitors affect the kinetics of both the anodic dissolution and, more pronouncedly, the cathodic reduction process.^{53,54} The EFM data validates the efficacy of the synthesized chitosan–ferrite nanocomposites as corrosion inhibitors for carbon steel in 1.0 M HCl. The inhibition efficiency is concentration-dependent, in the order **Chit-ZnFe₂O₄** > **Chit-CuFe₂O₄** > **Chit-SrFe₁₂O₁₉** at high concentrations, which is in agreement with the trends in PDP and is consistent with the physicochemical characteristics of the included ferrite nanoparticles. The EFM measurements also indicate a mixed-type inhibition mechanism with prevailing influence on the cathodic process.

3.2.3 Electrochemical impedance spectroscopy (EIS). EIS is useful for understanding the interfacial processes and resistive and capacitive behavior of the electrode–electrolyte system.^{55,56} The EIS data were fitted to a modified equivalent circuit, which comprises solution resistance (R_{s}), film resistance (R_{f}) and film capacitance (CPE_{f}), charge transfer resistance (R_{ct}), and double-layer capacitance (CPE_{dl}) (inset of Fig. 8). Low χ^2 values ($<10^{-3}$) indicate good agreement between the experimental data and the fitted equivalent circuit model.⁵⁷ The utilization of Constant Phase Elements (CPE) rather than pure capacitors explains the non-ideal behavior and surface heterogeneity widely encountered in corrosion systems.^{58,59} The representative Nyquist and

Bode plots for carbon steel in 1.0 M HCl with chitosan–ferrite nanocomposites are displayed in Fig. 8. Examination of Nyquist plots (Fig. 8a–c) shows drastic modification of impedance response with the addition of chitosan–ferrite nanocomposites. The blank solution shows one capacitive loop with a comparatively small diameter, which signifies low polarization resistance and high corrosion activity.⁶⁰ However, with the addition of chitosan–ferrite nanocomposites, the diameter of the capacitive loop increases considerably and increases with increasing concentration of the inhibitor. This directly signifies an increase in overall impedance of the system and represents the inhibitive effect of the composite.⁶¹ The loop shape further indicates the presence of more than one time constant, which corroborates the proposed equivalent circuit with both a film and a charge transfer resistance. The Bode plots (magnitude and phase angle, Fig. 8d–f) also complement these observations. The impedance magnitude ($|Z|$) at low frequencies rises significantly with chitosan–ferrite nanocomposites concentration, reinforcing the increased barrier properties.⁶² The phase angle plots exhibit a shift to more negative angles in the intermediate frequency range with increasing inhibitor concentration, pointing towards increasingly capacitive interfacial behavior and the formation of the protective film.^{63,64} The EIS parameters derived from fitting experimental data using the equivalent circuit are listed in Table 4. The solution resistance (R_{s}) is relatively constant for all measurements, as can be expected for a fixed concentration of the electrolyte. One of the main observations is the large increase in charge transfer resistance (R_{ct}) with increasing inhibitor concentration for all three composites. For example, for **Chit-ZnFe₂O₄**, R_{ct} rises from 19.05 $\Omega \text{ cm}^2$ for the blank to 646.42 $\Omega \text{ cm}^2$ at 400 ppm. This large increase in R_{ct} indicates a decrease in the rate of the charge transfer process (corrosion reaction), demonstrating the efficiency of the chitosan–ferrite nanocomposites.⁶⁵ At the same time, the double-layer capacitance (C_{dl} , calculated from CPE_{dl})



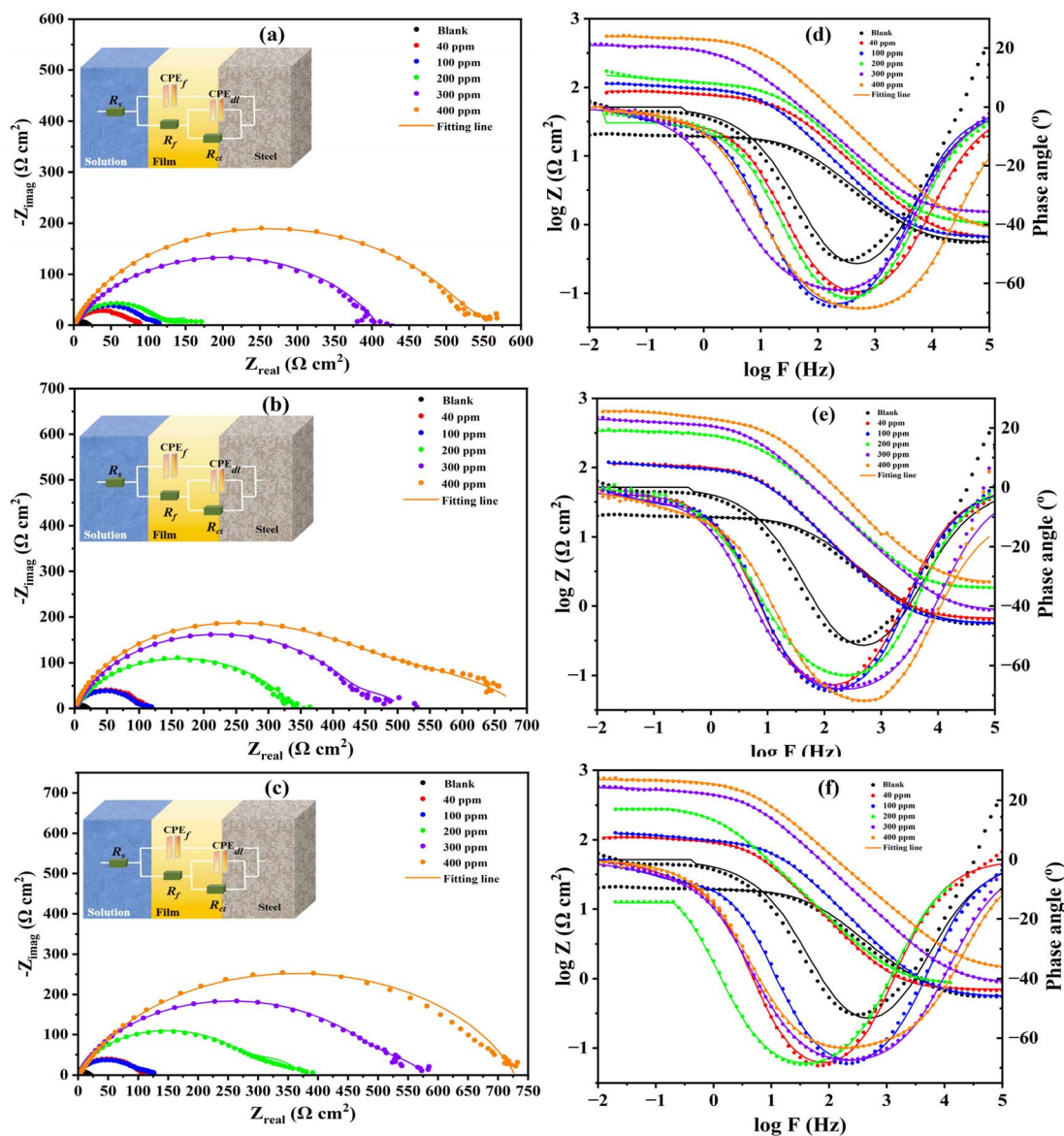


Fig. 8 Nyquist plots, Bode and phase angle plots for steel in 1.0 M HCl solution without and with different concentrations of (Chit-SrFe₁₂O₁₉ (a and d), Chit-CuFe₂O₄ (b and e) and Chit-ZnFe₂O₄ (c and f) composites at 30 °C.

decreases noticeably with increasing inhibitor concentration (e.g., from 406.90 $\mu\text{F cm}^{-2}$ for the blank to 28.39 $\mu\text{F cm}^{-2}$ for **Chit-ZnFe₂O₄** at 400 ppm). The decrease in C_{dl} is usually explained by the adsorption of inhibitor molecules on the metal surface, decreasing the effective area for charge transfer and/or thickening the electrical double layer by forming an adsorbed layer.^{66–69} The inhibition efficiency as determined using the EIS data $\eta_z\%$ (based on $[R_p = R_{ct} + R_f]$ values using the formula given in the Experimental section) follows the expected trend and increases with the concentration of the chitosan–ferrite nanocomposites. At the highest concentration examined (400 ppm), inhibition efficiencies of 97.16%, 97.29%, and 97.38% for **Chit-SrFe₁₂O₁₉**, **Chit-CuFe₂O₄**, and **Chit-ZnFe₂O₄**, respectively, were achieved. Such high efficiencies are a strong indication of the formation of efficient protective layers. Also, the surface

coverage values (θ) tend towards unity (0.9738 for **Chit-ZnFe₂O₄** at 400 ppm), reflecting almost complete surface coverage by the inhibitor film at the highest concentration. The EIS data also enables the examination of the properties of the film formed itself. The resistance of the film (R_f) is seen to increase appreciably with chitosan–ferrite nanocomposites concentration (e.g., from 13.90 $\Omega \text{ cm}^2$ for **Chit-ZnFe₂O₄** at 40 ppm to 79.91 $\Omega \text{ cm}^2$ for **Chit-ZnFe₂O₄** at 400 ppm), reflecting the formation of a resistive barrier layer. The values of film capacitance (C_f) are typically lower than C_{dl} , in line with the formation of a thicker, more dielectric layer than the electric double layer.⁷⁰ The EIS findings validate that the prepared chitosan–ferrite nanocomposites are good inhibitors for the corrosion of carbon steel in 1.0 M HCl through the formation of protective films. The inhibition efficiency is concentration-dependent for all



Table 4 EIS parameters for corrosion of steel in 1.0 M HCl in the absence and presence of different concentrations of (Chit-SrFe₁₂O₁₉, Chit-CuFe₂O₄ and Chit-ZnFe₂O₄) composites at 30 °C^a

Inhibitor	Conc. (ppm)	CPE _r					CPE _{dl}					R _p (R _f + R _{ct})	θ	η _i %	
		R _s (Ω cm ²)	R _f (Ω cm ²)	Y ₀₁ (μΩ ⁻¹ s ⁿ cm ⁻²)	n ₁	C _f (μF cm ⁻²)	R _{ct} (Ω cm ²)	Y ₀₂ (μΩ ⁻¹ s ⁿ cm ⁻²)	n ₂	C _{dl} (μF cm ⁻²)	Chi squared (χ ²)				
Blank	—	0.5409	—	—	—	—	19.05	736.27	0.8780	406.90	9.04 × 10 ⁻³	19.05	—	—	—
Chit-SrFe ₁₂ O ₁₉	40	0.6385	9.17	694.30	0.8789	346.00	79.56	689.00	0.8049	340.83	3.78 × 10 ⁻⁴	88.73	0.7853	78.53	—
	100	0.6649	16.55	520.40	0.8429	214.53	97.31	384.60	0.8717	237.14	6.29 × 10 ⁻⁴	113.86	0.8327	83.27	—
	200	1.0340	42.03	213.70	0.8338	83.53	113.55	221.60	0.8627	123.32	9.21 × 10 ⁻⁴	155.58	0.8775	87.75	—
	300	1.5000	56.40	116.90	0.8328	42.65	350.40	174.70	0.8627	111.98	3.39 × 10 ⁻⁴	406.80	0.9532	95.32	—
Chit-CuFe ₂ O ₄	400	0.8146	63.90	63.75	0.8131	17.99	607.93	126.00	0.8712	86.17	1.76 × 10 ⁻⁴	671.83	0.9716	97.16	—
	40	0.6408	12.62	607.50	0.8999	353.38	95.83	475.50	0.8819	314.43	8.62 × 10 ⁻⁴	108.45	0.8243	82.43	—
	100	0.5712	17.20	516.30	0.8466	219.36	97.37	384.30	0.9227	291.83	7.14 × 10 ⁻⁴	114.57	0.8337	83.37	—
	200	1.8370	44.08	144.10	0.9155	90.34	294.12	206.30	0.8624	131.90	2.67 × 10 ⁻⁴	338.20	0.9437	94.37	—
Chit-ZnFe ₂ O ₄	300	0.9596	59.55	87.82	0.9999	87.77	412.10	164.00	0.8716	110.28	4.14 × 10 ⁻³	471.65	0.9596	95.96	—
	400	0.8649	69.84	47.81	0.8518	17.73	633.66	108.60	0.8532	68.52	1.50 × 10 ⁻⁴	703.50	0.9729	97.29	—
	40	0.7041	13.90	571.50	0.8599	259.94	95.27	401.80	0.8999	279.50	9.57 × 10 ⁻⁴	109.17	0.8255	82.55	—
	100	0.5518	28.28	276.00	0.8408	110.12	96.30	291.50	0.8747	174.72	6.50 × 10 ⁻⁴	124.58	0.8471	84.71	—
200	0.8497	45.56	119.40	0.8254	39.63	321.55	199.10	0.8750	134.44	3.98 × 10 ⁻⁴	367.11	0.9481	94.81	—	
300	0.8728	62.18	64.99	0.7994	16.30	510.86	142.40	0.8713	96.70	7.07 × 10 ⁻⁴	573.04	0.9668	96.68	—	
400	1.3630	79.91	17.17	0.8087	3.61	646.42	47.50	0.8713	28.39	2.98 × 10 ⁻⁴	726.33	0.9738	97.38	—	

^a R_s = solution resistance, R_{ct} = charge transfer resistant, Y₀, n = constant phase elements, C_{dl} = double layer capacitance, θ = surface coverage, η_i = inhibition efficiency.

composites, with **Chit-ZnFe₂O₄** having the highest efficiency, followed by **Chit-CuFe₂O₄** and **Chit-SrFe₁₂O₁₉**. The EIS measurements establish that the inhibition process is through the formation of a resistive film (rise in R_f) that suppresses both electrolyte access and charge transfer (rise in R_{ct}), resulting in a notable decrease in corrosion. The surface area and morphology are the key physicochemical attributes of the individual ferrite nanoparticles that determine the overall composite inhibition performance.

3.2.4 Adsorption considerations. The degree of surface coverage (θ) gained from the electrochemical measurements (PDP, EFM, EIS) isotherm data fitted in several theoretical adsorption models, such as Langmuir, Freundlich, Temkin, Frumkin, Flory-Huggins, and El-Awady. The parameters and correlation coefficients (R²) for the different adsorption models are summarized in Table 5. The analysis of the various isotherm models indicates that the Langmuir model fits the adsorption data best, with the largest correlation coefficients (R² values close of 1 were determined) for all three composites.⁷¹ The linearized Langmuir plot (Fig. 9) of **Chit-ZnFe₂O₄**, **Chit-CuFe₂O₄** and **Chit-SrFe₁₂O₁₉**, shows excellent linearity of R² values of 0.9996, 0.9997, and 0.9995, respectively. The Langmuir model assumes monolayer adsorption of modest no interaction between the adsorbed species on a homogeneous surface with a finite number of identical sites. By using the linear plot of C/θ versus C, intercept provide the reciprocal of K_{ads}.⁷² The K_{ads} values calculated from the Langmuir model were 0.0782 M⁻¹, 0.0727 M⁻¹ and 0.0537 M⁻¹, for **Chit-ZnFe₂O₄**, **Chit-CuFe₂O₄**, and **Chit-SrFe₁₂O₁₉**, respectively. The corresponding standard free energy of adsorption (ΔG_{ads}^o) was calculated using the expression: ΔG_{ads}^o = -RT ln(10⁶ × K_{ads}), wherein R is the gas constant, T is the absolute temperature in degrees Kelvin (303 K), and 10⁶ ppm is the water concentration.⁷³ The resulting ΔG_{ads}^o values of -28.38 kJ mol⁻¹, -28.20 kJ mol⁻¹, and -27.44 kJ mol⁻¹ were for **Chit-ZnFe₂O₄**, **Chit-CuFe₂O₄**, and **Chit-SrFe₁₂O₁₉**, respectively. The negative values indicate that the adsorption process is spontaneous.⁷⁴ The magnitude of ΔG_{ads}^o values from -20 to -40 kJ mol⁻¹ indicates the adsorptive process involved physical adsorption (physisorption, that is, by electrostatic interaction) and chemical adsorption (chemisorption, which can be thought of as charge sharing or transfer) involving the chitosan-ferrite nanocomposites and the metal surface.⁷⁵ The higher fit of the Langmuir model for all three composites provides solid evidence that the chitosan-ferrite composites form a monolayer on the carbon steel surface. The order of calculated K_{ads} and the magnitudes of ΔG_{ads}^o (**Chit-ZnFe₂O₄** > **Chit-CuFe₂O₄** > **Chit-SrFe₁₂O₁₉**) correlated well with the achieved inhibition efficiencies and the physico-chemical properties of the ferrite nanoparticles.

3.3 Global reactivity parameters

The standard set of global reactivity descriptors provides a practical framework for assessing the fundamental characteristics of chemical compounds under study.⁷⁶ These parameters are valuable for comparing structures and drawing essential insights into their chemical reactivity and



Table 5 Adsorption isotherms models of the inhibitors with values of R^2 , slopes, intercepts, K_{ads} , and ΔG_{ads} obtained by using data from electrochemical measurements^a

Adsorption isotherm model	Linear form equation	Technique	Inhibitor	Slope	Intercept	R^2	$K_{\text{ads}} \text{ M}^{-1}$	$\Delta G_{\text{ads}} \text{ kJ mol}^{-1}$
Freundlich	$\log \theta = \log K + 1/n \log C$	PDP	Chit-SrFe ₁₂ O ₁₉	0.10810	-0.28294	0.97877	0.5213	-33.16
			Chit-CuFe ₂ O ₄	0.10535	-0.27330	0.97736	0.5330	-33.22
			Chit-ZnFe ₂ O ₄	0.09774	-0.25275	0.95955	0.5588	-33.34
Langmuir	$\frac{c}{\theta} = \frac{1}{K} + c$	EFM	Chit-SrFe ₁₂ O ₁₉	0.89962	73.84235	0.99019	0.0135	-23.97
			Chit-CuFe ₂ O ₄	0.94619	49.12175	0.98715	0.0204	-24.99
			Chit-ZnFe ₂ O ₄	0.94931	42.64592	0.99396	0.0234	-25.35
		EIS	Chit-SrFe ₁₂ O ₁₉	0.99261	18.61154	0.99769	0.0537	-27.44
			Chit-CuFe ₂ O ₄	0.99553	13.76444	0.99916	0.0727	-28.20
			Chit-ZnFe ₂ O ₄	0.99480	12.78497	0.99938	0.0782	-28.38
		PDP	Chit-SrFe ₁₂ O ₁₉	0.97828	16.02054	0.99950	0.0624	-27.82
			Chit-CuFe ₂ O ₄	0.97708	14.85207	0.99967	0.0673	-28.01
			Chit-ZnFe ₂ O ₄	0.97858	13.40201	0.99960	0.0746	-28.27
Frumkin	$\log \frac{\theta}{(1-\theta)C} = \log K + 2a\theta$	PDP	Chit-SrFe ₁₂ O ₁₉	1.18111	-2.10323	0.40612	7.8844×10^{-3}	-22.60
			Chit-CuFe ₂ O ₄	1.46607	-2.31054	0.51726	4.8917×10^{-3}	-21.40
			Chit-ZnFe ₂ O ₄	1.74358	-2.51981	0.58694	3.0213×10^{-3}	-20.19
Temkin	$\theta = -\frac{1}{2a} \ln C - \frac{1}{2a} \ln K$	PDP	Chit-SrFe ₁₂ O ₁₉	10.28473	-4.24152	0.97753	0.6621	-33.76
			Chit-CuFe ₂ O ₄	10.49258	-4.50646	0.97792	0.6508	-33.72
			Chit-ZnFe ₂ O ₄	10.97046	-5.02587	0.95867	0.6325	-33.65
Flory-Huggins	$\log \left(\frac{\theta}{c} \right) = \log K + n \log(1-\theta)$	PDP	Chit-SrFe ₁₂ O ₁₉	0.72422	-1.36808	0.92221	4.2847×10^{-2}	-26.87
			Chit-CuFe ₂ O ₄	0.69302	-1.36228	0.94004	4.3423×10^{-2}	-26.90
			Chit-ZnFe ₂ O ₄	0.68194	-1.33621	0.93478	4.6110×10^{-2}	-27.05
El-Awady	$\log \left(\frac{\theta}{1-\theta} \right) = \log K + y \log c$	PDP	Chit-SrFe ₁₂ O ₁₉	1.24518	-1.57383	0.93477	0.054457	-27.47
			Chit-CuFe ₂ O ₄	1.31841	-1.67360	0.94854	0.053777	-27.44
			Chit-ZnFe ₂ O ₄	1.33708	-1.65761	0.94447	0.057581	-27.61

^a R^2 = regression correlation coefficient, K = binding constant, θ = surface coverage, c = concentration.

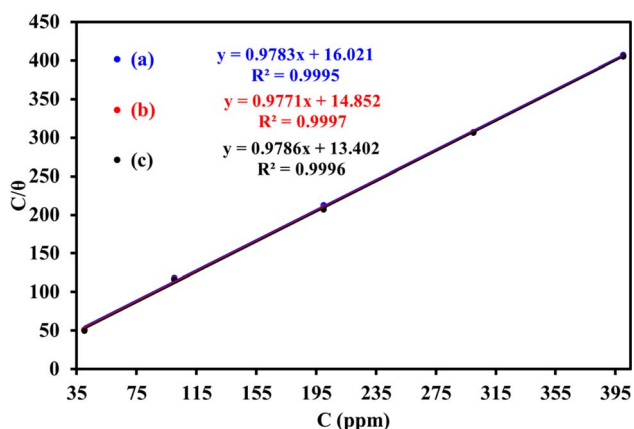


Fig. 9 The Langmuir adsorption model for (Chit-SrFe₁₂O₁₉) (a), Chit-CuFe₂O₄ (b) and Chit-ZnFe₂O₄ (c) composites on the steel surface in 1.0 M HCl using data obtained from PDP measurements at 30 °C.

thermodynamic stability. The descriptors are derived from the electronic structure of the molecule, specifically the energies of the highest occupied (HOMO) and lowest unoccupied (LUMO) molecular orbitals.⁷⁷ The ionization potential is defined as the minimum energy needed to remove the highest-energy electron from an isolated molecule. The electron affinity describes the accommodation of an excess electron corresponding to the LUMO energy. Molecular electronegativity is calculated as follows:

$$\chi = -\frac{1}{2}(E_{\text{HOMO}} + E_{\text{LUMO}}). \quad (3)$$

The electronic chemical potential equals:

$$\mu = \frac{1}{2}(E_{\text{HOMO}} + E_{\text{LUMO}}). \quad (4)$$

The chemical hardness and chemical softness originate from the ionization potential, I , and electron affinity, A :

$$\eta = \frac{1}{2}(I - A); \quad S = \frac{1}{2}(A - I). \quad (5)$$

The system's electrophilicity index equals:

$$\omega = \frac{1}{2}\mu^2\sigma. \quad (6)$$

In this work, the DFT calculations were used to characterize the intrinsic electronic structure of representative chitosan/ferrite fragments in aqueous environment, rather than to reproduce individual electrochemical observables. Global reactivity descriptors, band gap, chemical hardness/softness, and electronegativity together with population analysis quantify the tendency of the respective units to donate and accept charge and identify the most nucleophilic and electrophilic regions that are expected to interact with the steel surface and aggressive ionic species. These quantities are defined for isolated molecular units. The inhibitor formulations studied were



Table 6 Global reactivity parameters – ionization potential, electron affinity, electronegativity, and electronic chemical potential – for the NP + chitosan systems

Nanoparticle	Ionization potential, eV	Electron affinity, eV	Electronegativity, eV	Electronic chemical potential, eV
CuFe ₂ O ₄	9.003	4.397	2.303	−2.303
ZnFe ₂ O ₄	7.734	3.541	2.096	−2.096
SrFe ₂ O ₄	7.553	3.116	2.218	−2.218
SrFe ₁₂ O ₁₉	9.111	4.386	2.363	−2.363

unrevealed to be chemically similar, so the numerical variation in the computed band gaps and hardness values is relatively small compared with the experimental scatter of the electrochemical data. To recapitulate, no formal regression between global reactivity descriptors and impedance or polarization parameters was attempted. Instead, the DFT results are interpreted qualitatively and comparatively.

Table 6 presents a set of parameters determined for the computed systems composed of the NPs and chitosan monomer (Fig. 10). SrFe₁₂O₁₉ (9.111 eV) and CuFe₂O₄ (9.003 eV) have the highest IP values, meaning it is harder to remove an electron

from these systems compared to ZnFe₂O₄ (7.734 eV) and SrFe₂O₄ (7.553 eV). This indicates slightly stronger electron binding in SrFe₁₂O₁₉ and CuFe₂O₄.⁷⁸ It is consistent with the observed electronic stabilization. CuFe₂O₄ (4.397 eV) and SrFe₁₂O₁₉ (4.386 eV) have the highest EA values, reflecting their ready acceptance of the electron. ZnFe₂O₄ and SrFe₂O₄ show lower affinities, suggesting less tendency toward reduction. SrFe₁₂O₁₉ (2.363 eV) and CuFe₂O₄ (2.303 eV) are more electronegative than ZnFe₂O₄ (2.096 eV). This observation indicates a stronger electron-attracting capability of the structure. Electronic chemical potential (μ) is, expectedly, negative in all cases.

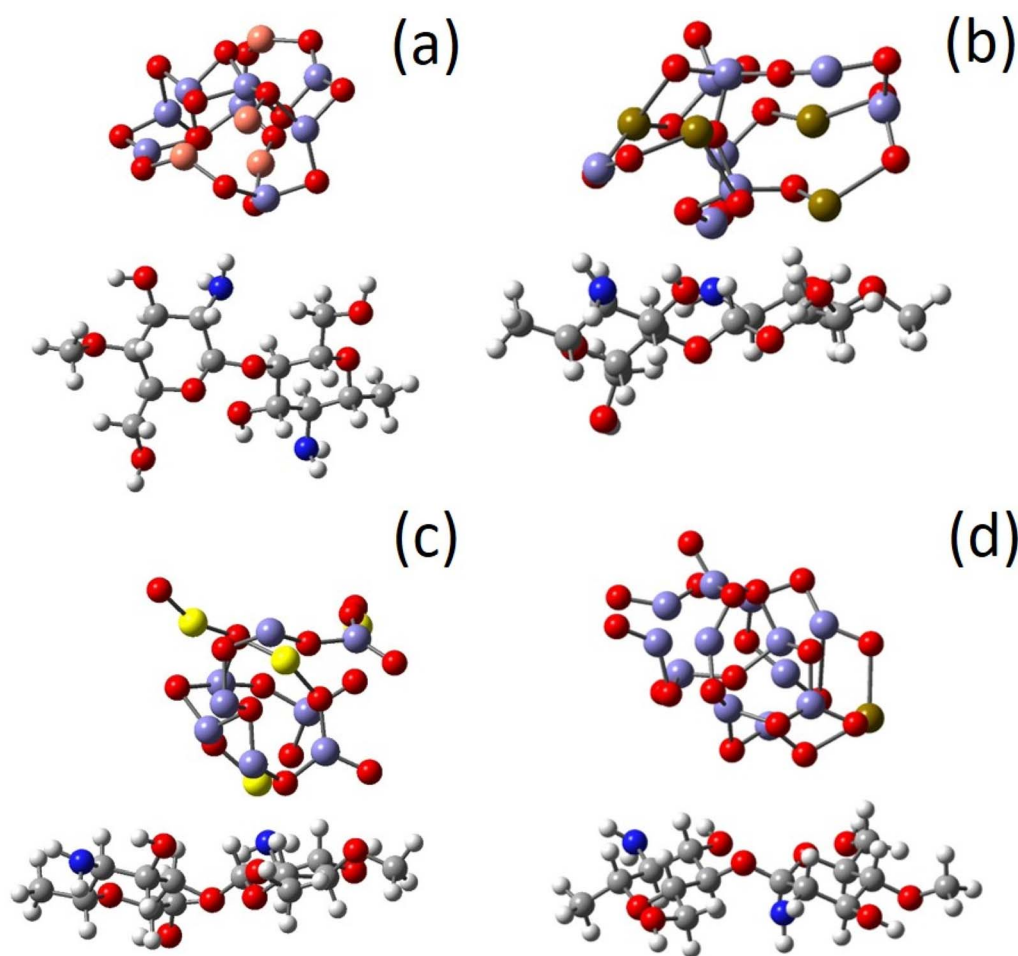


Fig. 10 The optimized structures of CuFe₂O₄ nanoparticle + chitosan (a), SrFe₂O₄ nanoparticle + chitosan (b), ZnFe₂O₄ nanoparticle + chitosan (c), SrFe₁₂O₁₉ nanoparticle + chitosan (d). The copper atoms are rosy, the strontium atoms are brown, the iron atoms are violet, the zinc atoms are yellow, the oxygen atoms are red, the carbon atoms are grey, and the hydrogen atoms are white.



Table 7 Global reactivity parameters – global chemical softness, global chemical hardness, electrophilicity index, and band gap – computed for the investigated systems

NP	Global chemical softness, eV^{-1}	Global chemical hardness, eV	Electrophilicity index, eV	Band gap, eV
CuFe_2O_4	0.217	2.303	1.152	4.606
ZnFe_2O_4	0.239	2.096	1.048	4.193
SrFe_2O_4	0.225	2.218	1.109	4.437
$\text{SrFe}_{12}\text{O}_{19}$	0.212	2.363	1.181	4.725

Herewith, $\text{SrFe}_{12}\text{O}_{19}$ has the most negative μ , and therefore must gain extra electron density to decrease the potential energy.

Table 7 summarizes additional global reactivity descriptors. Hardness reflects resistance to charge transfer. $\text{SrFe}_{12}\text{O}_{19}$ (2.363 eV) and CuFe_2O_4 (2.303 eV) are the hardest species, while ZnFe_2O_4 (2.096 eV) is the softest. This suggests ZnFe_2O_4 is more chemically reactive due to easier charge redistribution.⁷⁹ Global chemical softness is inversely related to hardness. Thus, ZnFe_2O_4 (0.239 eV^{-1}) is the softest (most polarizable and reactive). On the contrary, $\text{SrFe}_{12}\text{O}_{19}$ is the hardest (0.212 eV^{-1}) out of the investigated set. Note that the observed differences are fairly modest.

Electrophilicity index reflects the system's ability to accept electrons. Values are all in the range 1.05–1.18 eV. CuFe_2O_4 and $\text{SrFe}_{12}\text{O}_{19}$ appeared to be slightly more electrophilic. This observation aligns with their high electron affinities discussed above. $\text{SrFe}_{12}\text{O}_{19}$ exhibits the widest band gap (4.725 eV), making it relatively insulating and least conductive. Whereas ZnFe_2O_4 has the narrowest band gap (4.193 eV), making it relatively electronically active in terms of possible semiconductor behavior. Yes, the analysis of the global reactivity parameters confirms that all four systems exhibit similar performance in the context of their chemical activities against a corrosion promoter.

The spatial distribution of the frontier molecular orbitals was analyzed (Fig. 10–12). The analysis revealed distinct

localization patterns depending on the nanoparticle's composition. In the CuFe_2O_4 + chitosan system (Fig. 11), the HOMO ($E_{\text{HOMO}} = -9.003 \text{ eV}$) is localized on the organic chitosan fragment, while the LUMO ($E_{\text{LUMO}} = -4.397 \text{ eV}$) is centered on the inorganic nanoparticle. This indicates that chitosan acts as an electron donor, and the copper nanoparticle acts as an acceptor.^{80,81}

In contrast, the picture changes for the zinc and strontium systems. In both ZnFe_2O_4 + chitosan (Fig. 12) and SrFe_2O_4 + chitosan (Fig. 13), both orbitals—the HOMO ($E_{\text{HOMO}} = -7.734 \text{ eV}$ and -7.553 eV , respectively) and the LUMO ($E_{\text{LUMO}} = -3.541 \text{ eV}$ and -3.116 eV , respectively)—are localized predominantly on the inorganic nanoparticle core. In the strontium system, a minor contribution to the HOMO is observed on the nitrogen atom of chitosan. This distribution demonstrates that in these systems, the nanoparticle itself serves as both the donor and acceptor center, governing its interaction mechanism with the metal surface. The observed differences in orbital localization are consistent with the calculated global reactivity parameters and confirm the distinct nature of the inhibitory action of the investigated composites.

3.4 Electrostatic potential charges

Computed electrostatic potential (ESP) charges and Hirshfeld charges for the investigated NPs are collected in Tables 8 and 9 correspondingly. In the system SrFe_2O_4 + chitosan, the ESP

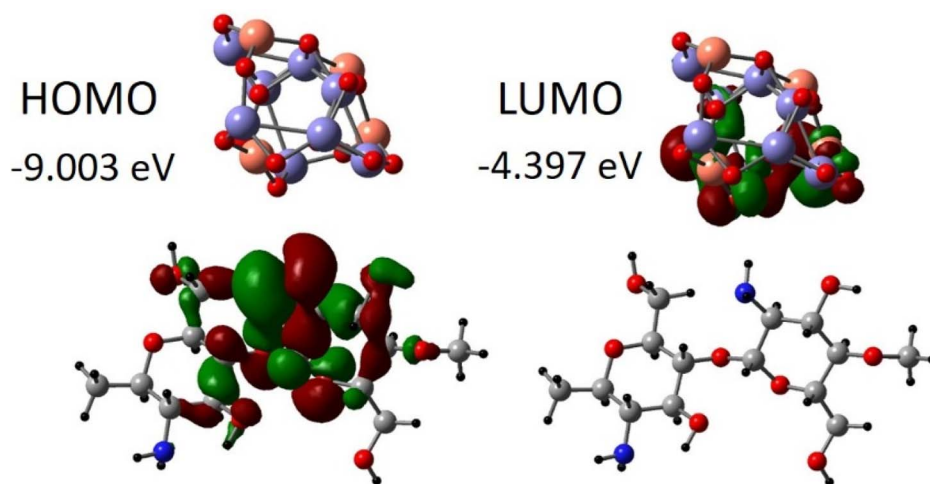


Fig. 11 The HOMO and LUMO distribution in CuFe_2O_4 nanoparticle + chitosan. The copper atoms are rosy, the iron atoms are violet, the oxygen atoms are red, the carbon atoms are grey, the nitrogen atoms are blue and the hydrogen atoms are black.



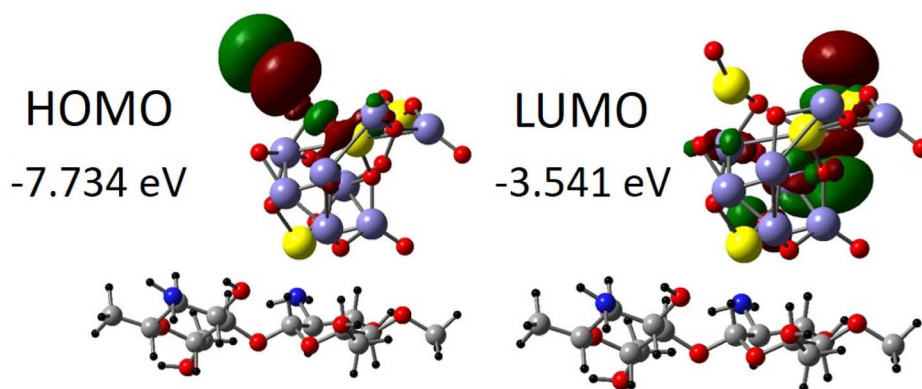


Fig. 12 The HOMO and LUMO distribution in ZnFe_2O_4 nanoparticle + chitosan. The zinc atoms are yellow, the iron atoms are violet, the oxygen atoms are red, the carbon atoms are grey, the nitrogen atoms are blue and the hydrogen atoms are black.

charges on Sr are $+1.526e$, $+1.615e$, $+1.619e$, and $+1.254e$ on the atom closest to the OH group of chitosan. The nearest oxygen in this OH group carries a charge of $-0.675e$. Compared to $-1.143e$ on the oxygen of the other OH group. The distance between the closest Sr and O atoms is 262 pm. On the Fe nanoparticle, the charges are $+0.699e$, $+0.778e$, $+0.921e$, $+0.955e$, $+1.073e$, $+1.638e$, and $+0.484e$. The Fe atom closest to the nitrogen of chitosan is nearly neutral, $+0.093e$. The corresponding N atom carries a charge of $+0.296e$. The distance between the nearest Fe and N atoms is 207 pm. The charges on the oxygen atoms of the NP range from $-0.613e$ to $-1.527e$.

The ESP charges on the Zn atoms in the system with ZnFe_2O_4 nanoparticle are $+1.267e$, $+1.330e$, and $+1.462e$. The closest Zn atom to the nitrogen of chitosan carries a charge of $+1.372e$. For

the Fe atoms in the nanoparticle, the charges are $+1.134e$, $+1.135e$, $+1.293e$, $+1.341e$, $+1.378e$, $+1.470e$, and $+1.652e$, with the Fe nearest to the hydrogen of chitosan's -OH group, having a charge of $+1.181e$. The hydrogen in this -OH group carries a charge of $-0.517e$, whereas the hydrogen in the remote -OH group, farther from the nanoparticle, has a charge of $+0.580e$. The $\text{Fe}\cdots\text{H}$ distance between the closest atoms is 249 pm. The oxygen atom with a charge of $-1.164e$ competes with Fe for the interaction with the same H, as evidenced by a shorter O-H distance of 197 pm. The charges on the oxygen atoms within the nanoparticle range from $-0.597e$ to $-1.629e$.

The ESP charges on the Cu atoms in the CuFe_2O_4 nanoparticle are $+0.786e$, $+1.078e$, $+1.152e$, and $+1.370e$. The charges on the Fe atoms are $+1.064e$, $+1.142e$, $+1.178e$, $+1.241e$, $+1.242e$,

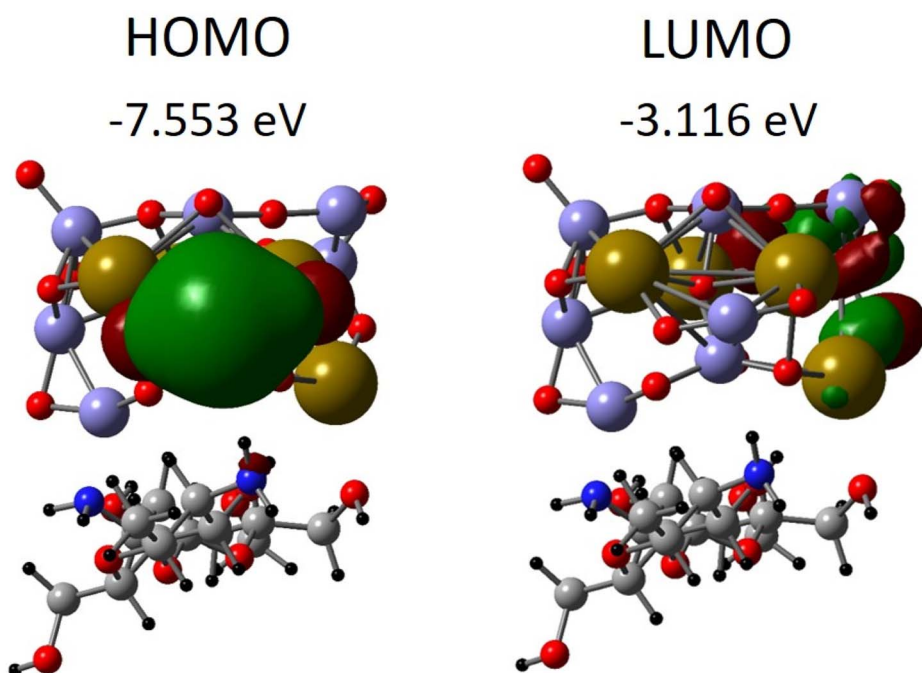


Fig. 13 The HOMO and LUMO distribution of SrFe_2O_4 nanoparticle + chitosan. The strontium atoms are brown, the iron atoms are violet, the oxygen atoms are red, the carbon atoms are grey, the nitrogen atoms are blue and the hydrogen atoms are black.



Table 8 Electrostatic potential charges (e) computed for the investigated nanoparticles

SrFe ₂ O ₄		
Sr	Fe	O
+1.619	+0.093	−0.188
+1.615	+1.073	−0.882
+1.254	+0.955	−0.613
+1.526	+0.921	−1.352
	+0.778	−1.527
	+1.638	−0.880
	+0.484	−1.021
	+0.699	−0.820
		−0.906
		−0.621
		−0.799
		−0.841
		−0.954
		−0.970
		−0.559
		−0.614
ZnFe ₂ O ₄		
Zn	Fe	O
+1.330	+1.134	−1.029
+1.372	+1.135	−1.136
+1.267	+1.652	−1.026
+1.462	+1.293	−0.597
	+1.341	−0.942
	+1.181	−0.745
	+1.378	−1.629
	+1.470	−0.876
		−1.221
		−0.947
		−1.164
		−1.048
		−0.672
		−1.121
		−0.862
		−1.066
CuFe ₂ O ₄		
Cu	Fe	O
+1.370	+1.284	−0.895
+1.152	+1.241	−0.699
+0.786	+1.284	−0.841
+1.078	+1.178	−0.944
	+1.142	−0.809
	+1.323	−0.847
	+1.242	−0.749
	+1.064	−1.210
		−0.893
		−0.849
		−0.854
		−1.033
		−0.817
		−1.002
		−1.084
		−0.680

Table 9 Hirshfeld charges (e) computed for the investigated nanoparticles

SrFe ₂ O ₄		
Sr	Fe	O
+0.532	+0.171	−0.303
+0.457	+0.401	−0.371
+0.521	+0.217	−0.254
+0.502	+0.413	−0.365
	+0.457	−0.263
	+0.579	−0.342
	+0.075	−0.447
	+0.418	−0.414
		−0.295
		−0.282
		−0.350
		−0.330
		−0.316
		−0.483
		−0.308
		−0.319
ZnFe ₂ O ₄		
Zn	Fe	O
+0.241	+0.398	−0.385
+0.505	+0.441	−0.366
+0.518	+0.506	−0.285
+0.592	+0.754	−0.325
	+0.667	−0.315
	+0.358	−0.422
	+0.237	−0.967
	+0.897	−0.356
		−0.418
		−0.382
		−0.324
		−0.322
		−0.378
		−0.508
		−0.332
		−0.404
CuFe ₂ O ₄		
Cu	Fe	O
+0.673	+0.529	−0.412
+0.607	+0.458	−0.314
+0.526	+0.404	−0.376
+0.596	+0.426	−0.411
	+0.351	−0.350
	+0.458	−0.415
	+0.377	−0.354
	+0.448	−0.334
		−0.373
		−0.362
		−0.378
		−0.369
		−0.294
		−0.462
		−0.315
		−0.338



+1.284e, +1.284e, and +1.323e. The charges on the oxygen atoms of the nanoparticle range from $-1.002e$ to $-0.699e$, with the oxygen closest to the $-NH_2$ group of chitosan carrying a charge of $-0.817e$. The corresponding atoms of this $-NH_2$ group exhibit charges of +0.616e (H), $-1.311e$ (N), and +0.485e (H). For comparison, the charges on a different $-NH_2$ group amount to $-1.059e$ (N), +0.449e (H), and +0.389e (H). The smallest distance between the NP (O site) and chitosan (H site) is 230 pm. The wide distribution of the ESP charges on the $SrFe_{12}O_{19}$ NP is exemplified by +1.488e on the Sr atom and +0.293e to +1.308e on the Fe atoms. The oxygen atoms in the nanoparticle possess charges varying from $-0.068e$ to $-0.867e$. The Sr is closest to the chitosan molecule, with distances to its hydrogen atoms amounting to 463 pm and 493 pm.

4. Conclusion

This study demonstrates the successful synthesis of $ZnFe_2O_4$, $CuFe_2O_4$, and $SrFe_{12}O_{19}$ nanoparticles *via* an ultrasound-assisted PEG route, yielding morphologically tailored ferrites with mesoporous characteristics. XRD analysis confirmed single-phase formation for $ZnFe_2O_4$ and $CuFe_2O_4$, while $SrFe_{12}O_{19}$ exhibited coexistence of hexagonal M-type ferrite and rhombohedral α - Fe_2O_3 , indicating a multiphase nature. Incorporation into chitosan-based nanocomposites enabled high-performance corrosion inhibition of carbon steel in acidic media, with inhibition efficiencies exceeding 98% at optimal concentration. The comprehensive electrochemical evaluation—spanning PDP, EFM, and EIS techniques—confirmed a mixed-type inhibition mechanism, predominantly impacting the cathodic process. Increased charge transfer resistance, reduced double-layer capacitance, and near-complete surface coverage underscore the formation of resistive protective films. Adsorption analyses supported spontaneous, monolayer composite-metal interactions with both physisorptive and chemisorptive contributions. Among the systems, **Chit-ZnFe₂O₄** exhibited the highest inhibition efficiency, attributed to its favorable textural properties and interfacial activity. These results validate the use of ultrasound-engineered ferrites as multifunctional additives for corrosion-resistant coatings and highlight their potential in advanced material formulations.

Author contributions

T. A., M. O., F. A.: conceptualization, methodology, investigation, synthesis, writing – original draft, resources. M. A. B., A. M. A., M. A. A.: electrochemical analysis, writing – review & editing, validation, visualization, data curation. N. A. A., V. V. C.: computational methodology, software, writing – original draft.

Conflicts of interest

The authors hereby declare no financial interests and professional connections that might bias the interpretations of the obtained results.

Data availability

The data supporting this article have been included in the publication.

Supplementary information (SI) is available. See DOI: <https://doi.org/10.1039/d5ra08173d>.

Acknowledgements

The authors are thankful to the Deanship of Graduate Studies and Scientific Research at the University of Bisha for supporting this work through the Fast-Track Research Support Program. The results of the work were obtained using the computational resources of Peter the Great Saint-Petersburg Polytechnic University Supercomputing Centre (<https://www.spbstu.ru/>). This work was also supported by the Deanship of Scientific Research, Vice Presidency for Graduate Studies and Scientific Research, King Faisal University, Saudi Arabia [Grant No. KFU260913]. During the preparation of this work the author(s) used QUILBOT to improve readability and language of the work. After using this tool/service, the author(s) reviewed and edited the content as needed and took(s) full responsibility for the content of the publication.

References

- 1 N. Sharma, Ferrite Nanoparticles for Corrosion Protection Applications, in *Engineered Ferrites and Their Applications*, ed. P. Sharma, G. K. Bhargava, S. Bhardwaj and I. Sharma, Springer Nature Singapore, Singapore, 2023, pp. 227–240, DOI: [10.1007/978-981-99-2583-4_12](https://doi.org/10.1007/978-981-99-2583-4_12).
- 2 M. Zain Ul Abidin, M. Ikram, S. Moeen, G. Nazir, M. B. Kanoun and S. Goumri-Said, A comprehensive review on the synthesis of ferrite nanomaterials via bottom-up and top-down approaches advantages, disadvantages, characterizations and computational insights, *Coord. Chem. Rev.*, 2024, **520**, 216158, DOI: [10.1016/j.ccr.2024.216158](https://doi.org/10.1016/j.ccr.2024.216158).
- 3 K. Shetty, L. Renuka, H. P. Nagaswarupa, H. Nagabhushana, K. S. Anantharaju, D. Rangappa, S. C. Prashantha and K. Ashwini, A comparative study on $CuFe_2O_4$, $ZnFe_2O_4$ and $NiFe_2O_4$: Morphology, Impedance and Photocatalytic studies, *Mater. Today Proc.*, 2017, **4**, 11806–11815, DOI: [10.1016/j.matpr.2017.09.098](https://doi.org/10.1016/j.matpr.2017.09.098).
- 4 M. Bohra, V. Alman and R. Arras, Nanostructured $ZnFe_2O_4$: An exotic energy material, *Nanomaterials*, 2021, **11**, 1286, DOI: [10.3390/nano11051286](https://doi.org/10.3390/nano11051286).
- 5 P. Shanker Sharma, K. Choudhary, V. K. Gupta and S. Kumar, Low-cost fabrication and characterization process for development of a sensitive optical fiber structure, *Appl. Opt.*, 2022, **61**, 8057–8063, DOI: [10.1364/AO.470687](https://doi.org/10.1364/AO.470687).
- 6 A. Kalendová and D. Veselý, The properties of $ZnFe_2O_4$ as an anticorrosion pigment dependent upon the structure of initial Fe_2O_3 , *Anti-Corros. Methods Mater.*, 2008, **55**, 175–190, DOI: [10.1108/00035590810887673](https://doi.org/10.1108/00035590810887673).
- 7 M. Azizi, M. Hussainzadeh and S. M. Saedi, Novel Hydrophobic, Anticorrosive, and Heat-Resistant



- CuFe₂O₄@Silicone-Based Resin Nanocomposites for Coating Applications, *J. Bio Tribocorros.*, 2025, **11**, 91, DOI: [10.1007/s40735-025-01008-6](https://doi.org/10.1007/s40735-025-01008-6).
- 8 A. Alneha, M. Hadi, H. Alnahari and A. Al-Sharabi, Optical, structural and antibacterial properties of phase heterostructured Fe(2)O(3)-CuO-CuFe(2)O(4) nanocomposite, *Sci. Rep.*, 2024, **14**, 14392, DOI: [10.1038/s41598-024-64090-9](https://doi.org/10.1038/s41598-024-64090-9).
- 9 M. Goli, M. Moradi and R. Dehghani Bidgoli, Green Synthesis of CuFe₂O₄ Nanoparticles Using Natural Extracts: Structural, Optical, and Magnetic Studies, *J. Electron. Mater.*, 2025, **54**, 2135–2145, DOI: [10.1007/s11664-025-11741-w](https://doi.org/10.1007/s11664-025-11741-w).
- 10 J. Ji, S. Zhang, C. Cao, S. Su, R. Jiang, A. Xia, H. Zhang, H. Li, Z. Liu and C. Jin, Structural and magnetic properties of SrFe₁₂O₁₉/CoFe₂O₄ composites with exchange coupling interaction, *J. Magn. Magn. Mater.*, 2022, **564**, 170073, DOI: [10.1016/j.jmmm.2022.170073](https://doi.org/10.1016/j.jmmm.2022.170073).
- 11 H. Qin, Y. He, P. Xu, D. Huang, Z. Wang, H. Wang, Z. Wang, Y. Zhao, Q. Tian and C. Wang, Spinel ferrites (MFe₂O₄): Synthesis, improvement and catalytic application in environment and energy field, *Adv. Colloid Interface Sci.*, 2021, **294**, 102486, DOI: [10.1016/j.cis.2021.102486](https://doi.org/10.1016/j.cis.2021.102486).
- 12 A. Soufi, H. Hajjaoui, R. Elmoubarki, M. Abdennouri, S. Qourzal and N. Barka, Spinel ferrites nanoparticles: Synthesis methods and application in heterogeneous Fenton oxidation of organic pollutants – A review, *Appl. Surf. Sci. Adv.*, 2021, **6**, 100145, DOI: [10.1016/j.apsadv.2021.100145](https://doi.org/10.1016/j.apsadv.2021.100145).
- 13 R. Chen, S. Ding and X. Ren, Preparation of ZnFe₂O₄@TiO₂ Novel Core-Shell Photocatalyst by Ultrasonic Method and Its Photocatalytic Degradation Activity, *Coatings*, 2022, **12**(10), 1407, DOI: [10.3390/coatings12101407](https://doi.org/10.3390/coatings12101407).
- 14 Meenu, P. Sharma, R. Purwar, N. Sharma, P. Rawat, S. R. Pathak, A. Thakur, H. Kim, M. Verma, S. Majumder and C. M. Srivastava, Ultrasonic Assisted Synthesis of CuFe₂O₄-Ag infused Gum Hydrogels Nanocomposite for photocatalytic Degradation of Organic Dye from Wastewater, *Water, Air, Soil Pollut.*, 2024, **235**(11), 690, DOI: [10.1007/s11270-024-07486-7](https://doi.org/10.1007/s11270-024-07486-7).
- 15 R. L. Palomino, A. M. Bolarín Miró, F. N. Tenorio, F. Sánchez De Jesús and C. A. Cortés, Sonochemical assisted synthesis of SrFe₁₂O₁₉ nanoparticles, *Ultrason. Sonochem.*, 2016, **29**, 470–475, DOI: [10.1016/j.ultsonch.2015.10.023](https://doi.org/10.1016/j.ultsonch.2015.10.023).
- 16 M. A. Bedair, E. H. Alosaimi and S. Melhi, A study of the inhibitive effect for corrosion of steel in 1.0 M HCl using a new nonionic surfactant based on coumarin moiety: chemical, electrochemical and quantum mechanics calculations, *J. Adhes. Sci. Technol.*, 2021, **37**, 1–31, DOI: [10.1080/01694243.2021.2018864](https://doi.org/10.1080/01694243.2021.2018864).
- 17 M. A. Bedair, A. M. Abuelela, M. Alshareef, M. Owda and E. M. Eliwa, Ethyl ester/acyl hydrazide-based aromatic sulfonamides: facile synthesis, structural characterization, electrochemical measurements and theoretical studies as effective corrosion inhibitors for mild steel in 1.0 M HCl, *RSC Adv.*, 2023, **13**, 186–211, DOI: [10.1039/D2RA05939H](https://doi.org/10.1039/D2RA05939H).
- 18 M. A. Bedair, A. M. Abuelela, S. Melhi, Q. A. Yousif, V. V. Chaban and E. H. Alosaimi, Highly effective inhibition of steel corrosion in 1.0 M HCl solution using a novel non-ionic surfactant with coumarin moiety: Practical and computational studies, *Mater. Chem. Phys.*, 2024, **312**, 128644, DOI: [10.1016/j.matchemphys.2023.128644](https://doi.org/10.1016/j.matchemphys.2023.128644).
- 19 J. P. Perdew, K. Burke and M. Ernzerhof, Generalized Gradient Approximation Made Simple, *Phys. Rev. Lett.*, 1996, **77**, 3865–3868, DOI: [10.1103/PhysRevLett.77.3865](https://doi.org/10.1103/PhysRevLett.77.3865).
- 20 P. Giannozzi, S. Baroni, N. Bonini, M. Calandra, R. Car, C. Cavazzoni, D. Ceresoli, G. L. Chiarotti, M. Cococcioni, I. Dabo, A. Dal Corso, S. de Gironcoli, S. Fabris, G. Fratesi, R. Gebauer, U. Gerstmann, C. Gougoussis, A. Kokalj, M. Lazzeri, L. Martin-Samos, N. Marzari, F. Mauri, R. Mazzarello, S. Paolini, A. Pasquarello, L. Paulatto, C. Sbraccia, S. Scandolo, G. Sclauzero, A. P. Seitsonen, A. Smogunov, P. Umari and R. M. Wentzcovitch, QUANTUM ESPRESSO: a modular and open-source software project for quantum simulations of materials, *J. Phys.: Condens. Matter*, 2009, **21**, 395502, DOI: [10.1088/0953-8984/21/39/395502](https://doi.org/10.1088/0953-8984/21/39/395502).
- 21 S. Grimme, J. Antony, S. Ehrlich and H. Krieg, A consistent and accurate ab initio parametrization of density functional dispersion correction (DFT-D) for the 94 elements H-Pu, *J. Chem. Phys.*, 2010, **132**, 154104, DOI: [10.1063/1.3382344](https://doi.org/10.1063/1.3382344).
- 22 R. Peverati and D. G. Truhlar, Performance of the M11-L density functional for bandgaps and lattice constants of unary and binary semiconductors, *J. Chem. Phys.*, 2012, **136**, 134704, DOI: [10.1063/1.3698285](https://doi.org/10.1063/1.3698285).
- 23 U. C. Singh and P. A. Kollman, An approach to computing electrostatic charges for molecules, *J. Comput. Chem.*, 1984, **5**, 129–145, DOI: [10.1002/jcc.540050204](https://doi.org/10.1002/jcc.540050204).
- 24 T. Risthaus and S. Grimme, Benchmarking of London Dispersion-Accounting Density Functional Theory Methods on Very Large Molecular Complexes, *J. Chem. Theory Comput.*, 2013, **9**, 1580–1591, DOI: [10.1021/ct301081n](https://doi.org/10.1021/ct301081n).
- 25 M. J. Frisch, G. W. Trucks, H. B. Schlegel, G. E. Scuseria, M. A. Robb, J. R. Cheeseman, G. Scalmani, V. Barone, G. A. Petersson, H. Nakatsuji, X. Li, M. Caricato, A. V. Marenich, J. Bloino, B. G. Janesko, R. Gomperts, B. Mennucci, H. P. Hratchian, J. V. Ortiz, A. F. Izmaylov, J. L. Sonnenberg, D. Williams-Young, F. Ding, F. Lipparini, F. Egidi, J. Goings, B. Peng, A. Petrone, T. Henderson, D. Ranasinghe, V. G. Zakrzewski, J. Gao, N. Rega, G. Zheng, W. Liang, M. Hada, M. Ehara, K. Toyota, R. Fukuda, J. Hasegawa, M. Ishida, T. Nakajima, Y. Honda, O. Kitao, H. Nakai, T. Vreven, K. Throssell, J. A. Jr, J. E. Peralta, F. Ogliaro, M. J. Bearpark, J. J. Heyd, E. N. Brothers, K. N. Kudin, V. N. Staroverov, T. A. Keith, R. Kobayashi, J. Normand, K. Raghavachari, A. P. Rendell, J. C. Burant, S. S. Iyengar, J. Tomasi, M. Cossi, J. M. Millam, M. Klene, C. Adamo, R. Cammi, J. W. Ochterski, R. L. Martin, K. Morokuma, O. Farkas, J. B. Foresman and D. J. Fox, *Gaussian 16, Revision C.01*, Gaussian Inc., Wallingford CT, 2016.



- 26 L. Faustino, B. McFadzean, J. Gouvêa Junior and L. Leal Filho, Bulk and Surface Characterization of Distinct Hematite Morphology: Implications for Wettability and Flotation Response, *Minerals*, 2024, **14**, 609, DOI: [10.3390/min14060609](https://doi.org/10.3390/min14060609).
- 27 R. Roshani and A. Tadjarodi, Synthesis of ZnFe₂O₄ nanoparticles with high specific surface area for high-performance supercapacitor, *J. Mater. Sci.: Mater. Electron.*, 2020, **31**, 23025–23036, DOI: [10.1007/s10854-020-04830-5](https://doi.org/10.1007/s10854-020-04830-5).
- 28 S. A. Jadhav, S. B. Somvanshi, M. V. Khedkar, S. R. Patade and K. M. Jadhav, Magneto-structural and photocatalytic behavior of mixed Ni–Zn nano-spinel ferrites: visible light-enabled active photodegradation of rhodamine B, *J. Mater. Sci.: Mater. Electron.*, 2020, **31**, 23025, DOI: [10.1007/s10854-020-03684-1](https://doi.org/10.1007/s10854-020-03684-1).
- 29 E. Tomina, L. Novikova, A. Kotova, A. Meshcheryakova, V. Krupskaya, I. Morozov, T. Koroleva, E. Tyupina, N. Perov and Y. Alekhina, ZnFe₂O₄/Zeolite Nanocomposites for Sorption Extraction of Cu²⁺ from Aqueous Medium, *AppliedChem*, 2023, **3**(4), 452, DOI: [10.3390/appliedchem3040029](https://doi.org/10.3390/appliedchem3040029).
- 30 S. S. Selima, M. Khairy and M. A. Mousa, Comparative studies on the impact of synthesis methods on structural, optical, magnetic and catalytic properties of CuFe₂O₄, *Ceram. Int.*, 2019, **45**, 6535–6540, DOI: [10.1016/j.ceramint.2018.12.146](https://doi.org/10.1016/j.ceramint.2018.12.146).
- 31 C. Cao, G. Yao, L. Jiang, M. Sokoluk, X. Wang, J. Ciston, A. Javadi, Z. Guan, I. De Rosa, W. Xie, E. J. Lavernia, J. M. Schoenung and X. Li, Bulk ultrafine grained/nanocrystalline metals via slow cooling, *Sci. Adv.*, 2019, **5**(8), 1–10, DOI: [10.1126/sciadv.aaw2398](https://doi.org/10.1126/sciadv.aaw2398).
- 32 N. T. K. Thanh, N. Maclean and S. Mahiddine, Mechanisms of Nucleation and Growth of Nanoparticles in Solution, *Chem. Rev.*, 2014, **114**, 7610–7630, DOI: [10.1021/cr400544s](https://doi.org/10.1021/cr400544s).
- 33 R. H. Kodama, Magnetic nanoparticles, *J. Magn. Magn. Mater.*, 1999, **200**, 359–372, DOI: [10.1016/S0304-8853\(99\)00347-9](https://doi.org/10.1016/S0304-8853(99)00347-9).
- 34 B. Huang, C. H. Bartholomew and B. F. Woodfield, Improved calculations of pore size distribution for relatively large, irregular slit-shaped mesopore structure, *Microporous Mesoporous Mater.*, 2014, **184**, 112–121, DOI: [10.1016/j.micromeso.2013.10.008](https://doi.org/10.1016/j.micromeso.2013.10.008).
- 35 W. J. Roth, B. Gil, W. Makowski, B. Marszalek and P. Eliášová, Layer like porous materials with hierarchical structure, *Chem. Soc. Rev.*, 2016, **45**, 3400–3438, DOI: [10.1039/C5CS00508F](https://doi.org/10.1039/C5CS00508F).
- 36 S. Liu, J. Zhou, G. Liang, X. Lyu and Y. Shi, Chitosan oligosaccharide derivatives as green corrosion inhibitors for 20# steel in 25 °C carbon dioxide environments, *Gas Sci. Eng.*, 2025, **143**, 205738, DOI: [10.1016/j.jgsce.2025.205738](https://doi.org/10.1016/j.jgsce.2025.205738).
- 37 M. A. Bedair, H. M. Elaryian, E. S. Gad, M. Alshareef, A. H. Bedair, R. M. Aboushahba and A. E.-A. S. Fouda, Insights into the adsorption and corrosion inhibition properties of newly synthesized diazinyll derivatives for mild steel in hydrochloric acid: synthesis, electrochemical, SRB biological resistivity and quantum chemical calculations, *RSC Adv.*, 2023, **13**, 478–498, DOI: [10.1039/D2RA06574F](https://doi.org/10.1039/D2RA06574F).
- 38 M. H. Esmail, H. A. Basuony, M. K. Al-Nawasany, M. M. Shulkamy, I. A. Shaaban, A. M. Abuelela, W. M. Zoghaib and T. A. Mohamed, Thiadiazole-2-Thiol-5-Thione and 2,5-Dimercapto-1,3,4-Thiadiazol Tautomerism, Conformational Stability, Vibrational Assignments, Inhibitor Efficiency and Quantum Chemical Calculations, *Z. Phys. Chem.*, 2020, **234**(3), 415–440, DOI: [10.1515/zpch-2018-1346](https://doi.org/10.1515/zpch-2018-1346).
- 39 N. Ben Seddik, A. Assafi, L. Hejji, Y. Zarki, Y. Aoulad El Hadj Ali, N. Raza, L. Pérez-Villarejo and A. Azzouz, Cysteine-modified graphene oxide as an efficient corrosion inhibitor for brass: Experimental and computational insights, *Diam. Relat. Mater.*, 2025, **158**, 112630, DOI: [10.1016/j.diamond.2025.112630](https://doi.org/10.1016/j.diamond.2025.112630).
- 40 P. Kumar, I. Soni, G. Kudur Jayaprakash, S. Kumar, S. Rao, R. Flores-Moreno and A. S. Sowmyashree, Experimental and theoretical studies of hexylmethylimidazolium tetrafluoroborate ionic liquid as cathodic corrosion inhibitor for mild steel, *Inorg. Chem. Commun.*, 2022, **146**, 110110, DOI: [10.1016/j.inoche.2022.110110](https://doi.org/10.1016/j.inoche.2022.110110).
- 41 N. Anusuya, J. Saranya, V. S. Angulakshmi, K. Vagdevi and A. Zarrouk, Experimental and Computational studies on the prevention of mild steel in sulphuric acid medium using bis-pyrimidine derivatives as corrosion inhibitors, *J. Mol. Struct.*, 2025, **1346**, 143134, DOI: [10.1016/j.molstruc.2025.143134](https://doi.org/10.1016/j.molstruc.2025.143134).
- 42 H. M. Elaryian, M. A. Bedair, A. H. Bedair, R. M. Aboushahba and A. E.-A. S. Fouda, Corrosion mitigation for steel in acid environment using novel p-phenylenediamine and benzidine coumarin derivatives: synthesis, electrochemical, computational and SRB biological resistivity, *RSC Adv.*, 2022, **12**, 29350–29374, DOI: [10.1039/D2RA05803K](https://doi.org/10.1039/D2RA05803K).
- 43 H. Hosseinzadeh, H. Oveisi and A. Meshkini, Comprehensive analysis of morphological effects in single and multi-layer zinc oxide and silica coatings on the physicochemical and biological properties of ZnFe₂O₄ nanoparticles, *Colloids Surf. A Physicochem. Eng. Asp.*, 2025, **718**, 136946, DOI: [10.1016/j.colsurfa.2025.136946](https://doi.org/10.1016/j.colsurfa.2025.136946).
- 44 Z. M. Abdulhamid, A. A. Dabbawala, T. Delclos, R. Straubinger, M. Rueping, K. Polychronopoulou and D. H. Anjum, Synthesis, characterization, and preliminary insights of ZnFe₂O₄ nanoparticles into potential applications, with a focus on gas sensing, *Sci. Rep.*, 2023, **13**, 19705, DOI: [10.1038/s41598-023-46960-w](https://doi.org/10.1038/s41598-023-46960-w).
- 45 T. Rodríguez-Flores, F. Shafiq and R. Nisticò, Synthesis, properties, and application in catalysis of Cu, Ni, Co, Zn ferrites: A comprehensive review study, *J. Alloys Compd.*, 2025, **1036**, 181926, DOI: [10.1016/j.jallcom.2025.181926](https://doi.org/10.1016/j.jallcom.2025.181926).
- 46 M. A. Bedair, M. M. B. El-Sabbah, A. S. Fouda and H. M. Elaryian, Synthesis, electrochemical and quantum chemical studies of some prepared surfactants based on azodye and Schiff base as corrosion inhibitors for steel in acid medium, *Corros. Sci.*, 2017, **128**, 54–72, DOI: [10.1016/j.corsci.2017.09.016](https://doi.org/10.1016/j.corsci.2017.09.016).



- 47 M. T. Abdullahi, S. A. Umoren, H. D. M. Dafalla and M. N. Tahir, Synthesis, characterization and anti-corrosion property of graphitic carbon nitride for carbon steel in acid medium, *Diam. Relat. Mater.*, 2025, **151**, 111819, DOI: [10.1016/j.diamond.2024.111819](https://doi.org/10.1016/j.diamond.2024.111819).
- 48 M. A. Bedair, S. A. Soliman, M. F. Bakr, E. S. Gad, H. Lgaz, I.-M. Chung, M. Salama and F. Z. Alqahtany, Benzidine-based Schiff base compounds for employing as corrosion inhibitors for carbon steel in 1.0 M HCl aqueous media by chemical, electrochemical and computational methods, *J. Mol. Liq.*, 2020, **317**, 114015, DOI: [10.1016/j.molliq.2020.114015](https://doi.org/10.1016/j.molliq.2020.114015).
- 49 A. El Amri, A. Hmada, F. El hajri, A. El Amri, M. Chafiq, A. Chaouiki, Y. G. Ko, S. Boukhris, M. Ebn-Touhami and N. Dkhireche, Development of anti-corrosive layer on steel alloy using quinoline-based inhibitor: Comprehensive experimental, characterization and DFT/DFTB perspectives, *Mater. Today Commun.*, 2025, **44**, 112082, DOI: [10.1016/j.mtcomm.2025.112082](https://doi.org/10.1016/j.mtcomm.2025.112082).
- 50 A. A. Aleid, M. M. Solomon, P. S. Umoren and S. A. Umoren, Evaluation of the effect of sodium alginate, hydroxyethyl cellulose, aspartame, and poly(ethylene oxide)-b-poly(propylene oxide) copolymer on the in-vitro corrosion of AZ31 Mg alloy in simulated body fluid, *Int. J. Biol. Macromol.*, 2025, **288**, 138749, DOI: [10.1016/j.ijbiomac.2024.138749](https://doi.org/10.1016/j.ijbiomac.2024.138749).
- 51 M. A. Bedair, Q. A. Yousif, Z. Fadel, S. Melhi, F. A. Al-Odail and A. M. Abuelela, Experimental and theoretical analyses of the corrosion inhibition efficacy of new penicillanic acid derivatives for carbon steel in hydrochloric acid environment, *J. Mol. Struct.*, 2025, **1328**, 141282, DOI: [10.1016/j.molstruc.2024.141282](https://doi.org/10.1016/j.molstruc.2024.141282).
- 52 Q. A. Yousif, M. A. Bedair, Z. Fadel, F. Al-Odail and A. M. Abuelela, Evaluating the efficacy of newly synthesized amino acid derivatives as corrosion inhibitors in acidic solutions, *Inorg. Chem. Commun.*, 2024, **164**, 112454, DOI: [10.1016/j.inoche.2024.112454](https://doi.org/10.1016/j.inoche.2024.112454).
- 53 E. H. Alosaimi, Some prepared schiff-base complexes for corrosion inhibition of steel in hydrochloric acid solution, *Mater. Chem. Phys.*, 2025, **333**, 130332, DOI: [10.1016/j.matchemphys.2024.130332](https://doi.org/10.1016/j.matchemphys.2024.130332).
- 54 M. A. Bedair, In-depth assessment of new coumarin derivative based on azo dye and Schiff base as an effective corrosion inhibitor for steel in 1 M HCl solution and anti sulphate reducing bacteria: Insights from computational and experimental techniques, *Inorg. Chem. Commun.*, 2024, **167**, 112693, DOI: [10.1016/j.inoche.2024.112693](https://doi.org/10.1016/j.inoche.2024.112693).
- 55 D. M. Jamil, H. S. Aljibori and A. Alamiery, Electrochemical analysis of 5-Nitro-2-furaldehyde semicarbazone as a mild steel corrosion inhibitor in corrosive solution: An EIS, adsorption and SEM study, *Results, Chem.*, 2025, **15**, 102193, DOI: [10.1016/j.rechem.2025.102193](https://doi.org/10.1016/j.rechem.2025.102193).
- 56 M. A. Abbas, E. I. Arafa, M. A. Bedair, A. S. Ismail, O. E. El-Azabawy, S. A. Baker and H. I. Al-Shafey, Synthesis, Characterization, Thermodynamic Analysis and Quantum Chemical Approach of Branched N, N'-bis(p-hydroxybenzoyl)-Based Propanediamine and Triethylenetetramine for Carbon Steel Corrosion Inhibition in Hydrochloric Acid Medium, *Arabian J. Sci. Eng.*, 2023, **48**, 7463–7484, DOI: [10.1007/s13369-022-07520-y](https://doi.org/10.1007/s13369-022-07520-y).
- 57 Q. A. Yousif, S. S. Malhotra, M. A. Bedair, A. Ansari and A. K. Hadi, Safflower plant extract as a sustainable corrosion inhibitor for carbon steel in acidic media: a combined electrochemical and computational study, *RSC Adv.*, 2025, **15**, 21006–21025, DOI: [10.1039/D5RA03333K](https://doi.org/10.1039/D5RA03333K).
- 58 S. N. El Houda and B. Amel, Eco-friendly green inhibitor for corrosion protection of API 5L X60 carbon steel in sulfuric acid solution, *J. Taiwan Inst. Chem. Eng.*, 2025, **173**, 106161, DOI: [10.1016/j.jtice.2025.106161](https://doi.org/10.1016/j.jtice.2025.106161).
- 59 A. M. Abuelela, M. A. Bedair, E. S. Gad, Y. F. El-Aryan, W. A. A. Arafa, A. K. Mourad, H. Nady and S. Eid, Exploring the synthesis, characterization, and corrosion inhibition of new tris-thiosemicarbazone derivatives for acidic steel settings using computational and experimental studies, *Sci. Rep.*, 2024, **14**, 13310, DOI: [10.1038/s41598-024-64199-x](https://doi.org/10.1038/s41598-024-64199-x).
- 60 M. A. Bedair, A novel coumarin-azo Schiff base for dual corrosion inhibition for steel in acidic environments and anti-SRB protection: Experimental and computational insights, *Results Surf. Interfaces*, 2025, **19**, 100511, DOI: [10.1016/j.rsurfi.2025.100511](https://doi.org/10.1016/j.rsurfi.2025.100511).
- 61 A. H. Al-Moubaraki, E. A. Noor, A. M. Khayaya, J. M. Al-Ahmari, A. A. Al-Ghamdi, F. M. Al Hayazi, M. Chafiq, A. Chaouiki and Y. G. Ko, Exploring factors affecting corrosion inhibition of mild steel using a quinolinium-based inhibitor: Experimental and theoretical approach, *J. Indian Chem. Soc.*, 2025, **102**, 101547, DOI: [10.1016/j.jics.2024.101547](https://doi.org/10.1016/j.jics.2024.101547).
- 62 M. Ragab and M. A. Bedair, The effect of permanent magnet stirring on the corrosion resistance of Sn-2.0Ag-0.5Cu-2Zn solder alloys in NaCl solution, *Mater. Chem. Phys.*, 2023, **302**, 127774, DOI: [10.1016/j.matchemphys.2023.127774](https://doi.org/10.1016/j.matchemphys.2023.127774).
- 63 A. M. Abuelela, J. Kaur, A. Saxena, M. A. Bedair, D. K. Verma and E. Berdimurodov, Electrochemical and DFT studies of Terminalia bellerica fruit extract as an eco-friendly inhibitor for the corrosion of steel, *Sci. Rep.*, 2023, **13**, 19367, DOI: [10.1038/s41598-023-45283-0](https://doi.org/10.1038/s41598-023-45283-0).
- 64 S. D. Kotabagi, S. K. Rajappa, R. L. Minagalavar, M. R. Rathod, J. G. Suma and A. M. Sajjan, Expired Lircetam drug as a corrosion inhibitor for low-carbon steel in 1 M HCl: Experimental, theoretical, and quantum chemical insights, *Results Surf. Interfaces*, 2025, **18**, 100459, DOI: [10.1016/j.rsurfi.2025.100459](https://doi.org/10.1016/j.rsurfi.2025.100459).
- 65 M. M. Y. Modwi, H. Feng, M. K. Hadi, N. Chen, J. Hou, E. Kamal and K. Yang, Eco-friendly corrosion inhibitor of Q235 carbon steel in 1.0 M HCl by Isatin/Chitosan Schiff base, *J. Mol. Struct.*, 2025, **1321**, 139592, DOI: [10.1016/j.molstruc.2024.139592](https://doi.org/10.1016/j.molstruc.2024.139592).
- 66 M. A. Bedair, S. A. Soliman and M. S. Metwally, Synthesis and characterization of some nonionic surfactants as corrosion inhibitors for steel in 1.0 M HCl (Experimental and computational study), *J. Ind. Eng. Chem.*, 2016, **41**, 10–22, DOI: [10.1016/j.jiec.2016.07.005](https://doi.org/10.1016/j.jiec.2016.07.005).



- 67 S. H. Bashir, M. M. Motawea, A. A. O. Younes, A. A. E. Satti, R. M. A. Daoub and M. F. Atia, Utilizing expired duloxetine as an eco-friendly corrosion inhibitor for API 5L X52 carbon steel in aqueous solutions: Experimental and computational analysis, *Results Chem.*, 2025, **16**, 102476, DOI: [10.1016/j.rechem.2025.102476](https://doi.org/10.1016/j.rechem.2025.102476).
- 68 M. A. Bedair, H. M. Elaryian, A. H. Bedair, R. M. Aboushabba, A. El-Aziz and S. Fouda, Novel coumarin-buta-1,3-diene conjugated donor-acceptor systems as corrosion inhibitors for mild steel in 1.0 M HCl: Synthesis, electrochemical, computational and SRB biological resistivity, *Inorg. Chem. Commun.*, 2023, **148**, 110304, DOI: [10.1016/j.inoche.2022.110304](https://doi.org/10.1016/j.inoche.2022.110304).
- 69 E. S. Gad, M. A. Abbas, M. A. Bedair, O. E. El-Azabawy and S. M. Mukhtar, Synthesis and applications of novel Schiff base derivatives as corrosion inhibitors and additives for improvement of reinforced concrete, *Sci. Rep.*, 2023, **13**, 15091, DOI: [10.1038/s41598-023-41165-7](https://doi.org/10.1038/s41598-023-41165-7).
- 70 O. Moumeni, M. Mehri, R. Kerkour, A. Boublia, F. Mihoub, K. Rebai, A. A. Khan, A. Erto, A. S. Darwish, T. Lemaoui, N. Chafai and Y. Benguerba, Experimental and detailed DFT/MD simulation of α -aminophosphonates as promising corrosion inhibitor for XC48 carbon steel in HCl environment, *J. Taiwan Inst. Chem. Eng.*, 2023, **147**, 104918, DOI: [10.1016/j.jtice.2023.104918](https://doi.org/10.1016/j.jtice.2023.104918).
- 71 K. Zaidi, H. Elmsellem, W. Daoudi, O. Dagdag, A. H. Al-Moubaraki, J. M. Al-Ahmari, H. Kim, A. Berisha, A. Aouniti, B. Dikici, R. Touzani and B. Hammouti, A novel methionine-based pyrazole derivative as a corrosion inhibitor in 1 M HCl: Experimental and theoretical insights, *Colloids Surf. A Physicochem. Eng. Asp.*, 2025, **726**, 137802, DOI: [10.1016/j.colsurfa.2025.137802](https://doi.org/10.1016/j.colsurfa.2025.137802).
- 72 S. Melhi, M. A. Bedair, E. H. Alosaimi, A. A. O. Younes, W. H. El-Shwiniy and A. M. Abuelela, Effective corrosion inhibition of mild steel in hydrochloric acid by newly synthesized Schiff base nano Co(II) and Cr(III) complexes: spectral, thermal, electrochemical and DFT (FMO, NBO) studies, *RSC Adv.*, 2022, **12**, 32488–32507, DOI: [10.1039/D2RA06571A](https://doi.org/10.1039/D2RA06571A).
- 73 A. M. Ashmawy, R. Said, I. A. Naguib, B. Yao and M. A. Bedair, Anticorrosion Study for Brass Alloys in Heat Exchangers during Acid Cleaning Using Novel Gemini Surfactants Based on Benzalkonium Tetrafluoroborate, *ACS Omega*, 2022, **7**, 17849–17860, DOI: [10.1021/acsomega.2c01119](https://doi.org/10.1021/acsomega.2c01119).
- 74 P. Shathani, E. N. Ogunmuyiwa, O. P. Oladijo and B. A. Obadele, Thermodynamics and adsorption behaviour of Sclerocarya birrea leaf extract as a potential green corrosion inhibitor for mild steel in a simulated seawater (3.5% NaCl) environment, *Chem. Thermodyn. Therm. Anal.*, 2025, **19**, 100197, DOI: [10.1016/j.ctta.2025.100197](https://doi.org/10.1016/j.ctta.2025.100197).
- 75 N. B. Iroha, C. U. Dueke-Eze, V. C. Anadebe, N. J. Maduelosi, R. Thomas and E. E. Ebenso, Assessment of a new benzylidene-based corrosion inhibitor for X60 carbon steel in 1 M HCl medium: Experimental and computational studies, *Results Surf. Interfaces*, 2025, **19**, 100510, DOI: [10.1016/j.rsurfi.2025.100510](https://doi.org/10.1016/j.rsurfi.2025.100510).
- 76 N. A. Andreeva, A. M. Abuelela, M. A. Alkhalifah, M. A. Bedair and V. V. Chaban, Binding corrosion promoters from aqueous solutions by Benzalkonium chloride, *J. Mol. Liq.*, 2025, **437**, 128583, DOI: [10.1016/j.molliq.2025.128583](https://doi.org/10.1016/j.molliq.2025.128583).
- 77 F. Al-Odail, M. A. Bedair, M. A. Alkhalifah and A. M. Abuelela, Comprehensive structural insights and electrochemical evaluation of rhamnose and salicin for green corrosion protection of carbon steel in acidic medium, *RSC Adv.*, 2025, **15**, 37429–37446, DOI: [10.1039/D5RA06243H](https://doi.org/10.1039/D5RA06243H).
- 78 Q. A. Yousif, M. A. Bedair, A. M. Abuelela, A. Ansari, S. S. Malhotra and Z. Fadel, High-performance corrosion inhibitors for carbon steel in hydrochloric acid: electrochemical and DFT studies, *RSC Adv.*, 2025, **15**, 28666–28688, DOI: [10.1039/D5RA04952K](https://doi.org/10.1039/D5RA04952K).
- 79 Q. A. Yousif, M. A. Bedair, A. M. Abuelela, A. Ansari and S. S. Malhotra, Structure-activity relationship of some prepared Schiff bases as corrosion inhibitors for carbon steel in hydrochloric acid: Experimental and DFT insights, *Mater. Today Commun.*, 2025, **49**, 113843, DOI: [10.1016/j.mtcomm.2025.113843](https://doi.org/10.1016/j.mtcomm.2025.113843).
- 80 M. Gab-Allah, M. Bedair, A. Elged, S. Soliman, E. Badr and M. Bakr, Empirical and Computational Investigation of Cationic Gemini Surfactants as Anti-Corrosive Inhibitors for Mild Steel in Acid Medium and its silver Nano Structure synthesis and Analysis., Egypt, *J. Chem.*, 2023, **66**(13), 2013–2031, DOI: [10.21608/ejchem.2023.222841.8256](https://doi.org/10.21608/ejchem.2023.222841.8256).
- 81 Q. A. Yousif, M. A. Bedair, A. M. Abuelela, F. Al-odail, A. Ansari and Z. Fadel, Theoretical and experimental aspects of novel penicillanic acid compounds as corrosion inhibitors in acidic solutions, *Mater. Today Commun.*, 2025, **47**, 113199, DOI: [10.1016/j.mtcomm.2025.113199](https://doi.org/10.1016/j.mtcomm.2025.113199).

